Synthesis of NiF 2 and NiF 2 ×4H 2 O Nanoparticles by Microemulsion and Their Self-Assembly

Hameed Ullah, Nicolas Batisse, Katia Guérin, Guillaume Rogez, Pierre Bonnet

To cite this version:

Hameed Ullah, Nicolas Batisse, Katia Guérin, Guillaume Rogez, Pierre Bonnet. Synthesis of NiF 2 and NiF 2 ×4H 2 O Nanoparticles by Microemulsion and Their Self-Assembly. Langmuir, 2020, 36 (29), pp.8461-8475. 10.1021/acs.langmuir.0c00889 . hal-02926198

HAL Id: hal-02926198

https://hal.science/hal-02926198

Submitted on 10 Nov 2020

Synthesis of NiF_2 and $NiF_2.4H_2O$ nanoparticles by microemulsion and their self-assembly

Hameed Ullah[1,2,3], *Nicolas Batisse*[1], *Katia Guerin*[1], *Guillaume Rogez*[4] *and Pierre Bonnet*[*][1]

[1] Institut de Chimie de Clermont-Ferrand, Université Clermont Auvergne, UMR 6296, BP 10448, F-63000 Clermont-Ferrand, France

[2] Department of Chemistry, Hazara University, Mansehra 21300, Pakistan

[3] Department of Chemistry, Islamia College Peshawar 25120, Pakistan

[4] Institut de Physique et Chimie des Matériaux de Strasbourg, University of Strasbourg, CNRS UMR 7504, BP 43, 67034 Strasbourg cedex 2, France

KEYWORDS: nickel fluoride, microemulsion, self-assembly, fluorination, nanoparticles

ABSTRACT. Super-structures or self-assembled nanoparticles open the development of new materials with improved and/or novel properties. Here, we present nickel fluoride (NiF_2) self-assemblies by successive preparatory methods. Originally, the self-assemblies were obtained by exploiting water-in-oil microemulsion technique as a result of auto-organization of hydrated

---

*Corresponding Authors e-mails: Pierre.M.Bonnet@uca.fr , hameedwazir@yahoo.co.uk

NiF_2 ($NiF_2.4H_2O$) nanoparticles. The nanostructuration of $NiF_2.4H_2O$ nanoparticles was confirmed from XRD and TEM data. The size and shape of $NiF_2.4H_2O$ nanoparticles, and their subsequent self-assemblies varied slightly as a function of water to surfactant and oil ratios. The SEM and TEM characterizations revealed that the nanoparticles are organized into a succession of self-assemblies: from individual nanoparticles assembled into layers to truncated bipyramids, which further auto-organized themselves into almond shaped super-structures. The anhydrous NiF_2 was achieved by heating $NiF_2.4H_2O$ self-assemblies under the dynamic flow of molecular fluorine (F_2) at moderate temperature (350°C). The preservation of self-assemblies during the transformation from $NiF_2.4H_2O$ to NiF_2 is successfully achieved. The obtained materials have specific surface areas (SSA) about 30 m^2/g, more than 60% the value for bulk NiF_2. The lithium ion (Li^+) storage capacities and mechanism of the nanostructured samples were tested and compared with the bulk material by galvanostatic cycling and X-Ray Absorption Spectroscopy (XAS). The nanostructured samples show higher capacities (~650 mAh/g) than the theoretical (554 mAh/g) first discharge capacity due to the concomitant redox conversion mechanism of NiF_2 and solid-electrolyte interphase (SEI) formation. The nanostructuration by self-assembly appears to positively influence the lithium diffusion in comparison with the bulk material. Finally, magnetic properties of nanostructured $NiF_2.xH_2O$ ($x = 0$, or 4) have been measured and appear to be very similar to the corresponding bulk materials, without any visible size-reduction effect. The hydrated samples $NiF_2.4H_2O$ show an antiferromagnetic ordering at $T_N = 3.8$ K, whereas the dehydrated ones (NiF_2) present a canted antiferromagnetic ordering at $T_N = 74$ K.

INTRODUCTION

Nanoscopic materials have been extensively explored – both on academic research and industrial levels – during the last couple of decades due to their novel and superior electrical, optical and structural properties over the conventional micro and macroscopic materials[1-8]. The characteristics of nanomaterials are primarily dependent on the size, shape and distribution of their nanoparticles[9-11]. Therefore, many materials have found renewed applications other than their classical uses. Assembling of particular size and shape nanoparticles into super architectures is critical for creation of functional nanomaterials having superior properties over the prevailing ones[12-14]. For example, ordered nanocrystals forming superlattices have been discovered for possible applications in magnetic and optical devices exploiting the quantum confinement effects[15-17]. Dense ceramics after sintering, and structures mimicking biomaterials are synthesized from ordered super-structures[18]. Furthermore, self-assembled nanoparticles have been explored for large number of technologically important materials – besides others – including metals, alloys, oxides, and organic-inorganic hybrids[19-22]. Self-assembling process is either controlled and/or self-propagating[23-24], and have been exploited for construction of super-structures of diverse materials through particularly designed synthesis protocols[25-29].

After their historical applications in metallurgy, isotopic separation and optics[30-32], interests in metal fluorides resurfaced at the turn of the century owing to their nanochemistry. This renewed attention has presented them as functional nanomaterials having applications in sensors, batteries, actuators, optical devices, optoelectronics and additives in lubricants besides others[33-36]. New methods have been developed for synthesis of metal fluorides nanoparticles and their self-assembled super-structures. Water-in-oil microemulsion method has been also exploited for preparation of metal fluoride nanostructures[37-38]. Besides the simplicity of reaction apparatus and low temperature processing, reverse microemulsion technique comes up with a large degree of freedom to effectively control size, shape, distribution and auto-organization of nanoparticles in the resulting materials by slightly varying the synthesis parameters[29, 39-42]. For example, self-assembled uniform nanoparticles of YF_3 have been prepared by water in cyclohexane reverse microemulsion using polyoxyethylene(5)isooctylphenyl ether (NP-5) as surfactant[43]. Randomly distributed BaF_2 nanoparticles were produced in a CTAB/water/isooctane reverse microemulsion[38].

The benefits of nanostructuration by self-assembly for functional transition metals fluorides could be very interesting. However, no attention is paid to the synthesis of nanostructurated metal fluorides by reverse microemulsion probably due to the formation of hydrated compounds, and difficulty in dehydration of the resulting nanomaterials. Among the metal fluorides, an important effort is done on FeF_3[44], but much less is done on compounds such as CoF_2 or NiF_2. Nevertheless, NiF_2 is attracting attention as conversion reaction material for Li ion batteries due to its comparatively high voltage (2.96 V) and specific capacity (554 mAh/g)[45]. However, its poor electronic conductivity, due to the high ionicity of Ni – F bond, is the main hurdle in its large scale applications as functional material in Li ion power storage devices[7]. Nonetheless, improvements in electrochemical properties of NiF_2 have been reported by doping with NiO, and also by preparation of nanocomposites with conductive carbon materials[46]. Furthermore, the electrochemical performances of NiF_2 nanomaterials could be improved by engineering self-assemblies having specific open facets as seen with CuO[47]. Besides the electrochemical interests in nanostructured NiF_2, the magnetic properties could also be interesting especially to see if NiF_2 could exhibit different magnetic properties upon nanostructuration[48].

Here we come up with a new strategy to synthesize self-assembled nanoparticles of anhydrous NiF_2. The final self-assembled super-structures were formed in a consequence to the successive auto-organization of different structures resulting of the individual nanoparticles auto-assembly in a CTAB/2-octanol/water reverse microemulsion system. The size and shape of self-assembled structures were controlled by varying the reaction duration, and water to surfactant (ω) and oil (α) molar ratios. The as synthesized $NiF_2.4H_2O$ nanomaterials were transformed to anhydrous NiF_2, by an original conversion method under gaseous molecular fluorine (F_2) while preserving their self-assembly. The transformation is achieved at significantly lower temperature than previously reported[49].

EXPERIMENTAL

MATERIALS

All the chemicals were purchased from commercial suppliers and used as such without further purification and/or treatments. The salts $Ni(NO_3)_2.6H_2O$, and $NiCl_2.6H_2O$ and NH_4F were purchased of Normapur-VWR and Sigma-Aldrich, respectively. The surfactant, cetyltrimethylammonium bromide (CTAB), was used of Acros Organics and the oil, 2-octanol, was used of Sigma-Aldrich. Ethanol, absolute and commercial, was purchased from Normapur-VWR.

MATERIALS CHARACTERIZATIONS

Powder X-Ray Diffraction (PXRD): XRD patterns of all the samples were recorded upon PANalytical XPERT-PRO diffractometer which was equipped with Cu Kα source (1.542Å) as monochromator diffraction beam and a linear detector X'celerator. The scanning of the diffraction beams was performed in continuous steps each of size 0.0840 2theta and counting time of 180 s. The crystallite size was estimated using the Scherrer's Equation (Eq. 1).

$$d = 0.94\lambda/\beta\cos\theta \qquad (1)$$

Where d corresponds to the crystallite and/or grain size, λ is the wavelength – here $\lambda = 1.542$Å – of the x-rays radiations used, β is the corrected width of the respective peak in radians at full width at half maximum (FWHM), and θ is the diffraction angle of the respective peak in degrees.

Raman and Infra-Red spectroscopies: Raman scattering spectra were measured upon Raman spectrometer of JobinYvon model T64000. The wavelength of laser was 514.5 nm (2.41 eV) and the power was set at 100 mW. The measurement was carried out in solid state by putting the sample powder upon glass slide under air at room temperature. The Fourier transformed Infrared (FTIR) spectra of all the samples were recorded in the mid IR regions upon Nicolet FTIR spectrometer from ThermoElectron Corporation in Attenuated Total Reflection (ATR) mode using SMART ORBIT accessory.

Thermogravimetry Analyses (TGA): TGA/DSC data of the hydrated nickel fluoride ($NiF_2.4H_2O$) samples were collected under inert nitrogen (N_2) environment in the range of 25°C to 800°C, at heating rate of 10°C/min using TGA analyzer of SETARAM Instrumentations (model Setsys Evolution).

77K nitrogen sorption analysis: Sorption isotherms of powder samples were measured to determine specific surface area (SSA), pore size and volume, and pore size distribution using

Micromeritics ASAP 2020. The samples were outgassed at room temperature for 24 hours prior surface area and porosity measurements.

Scanning Electronic Microscopy (SEM) and Transmission Electronic Microscopy (TEM): SEM images of the samples were taken using SUPRA 55VP ZEISS field-effect scanning electron microscope (FE-SEM) equipped with a Gemini® column and high efficiency secondary electron detector. The sample powders were dispersed upon carbon film and have been analyzed without further treatments. Samples were observed using a Hitachi Transmission Electron Microscope (H-7650) at 80 kV acceleration voltage with magnifications up to x200,000. Images were taken using a Hamamatsu camera placed in a side position. The powders of the materials are investigated by TEM are suspended in ethanol and dropped on a 400 mesh holey carbon-coated copper grid and dried at room temperature in air.

Magnetic Measurements (SQUID): SQUID data were collected on a Quantum Design MPMS3 magnetometer. Magnetization measurements at different fields at a given temperature confirmed the absence of ferromagnetic impurities. Data were corrected for the sample holder and diamagnetism was estimated using Pascal constants.

Electrochemical Measurements: The electrochemical performances were investigated using galvanostatic discharges. The electrodes were composed of active material (80% w/w), acetylene black (10% w/w) and polyvinylidene difluoride (PVDF 10% w/w) as binder. After stirring in propylene carbonate (PC), the mixture was spread uniformly onto a stainless steel current collector disk of 10 mm diameter. After the PC evaporation, the electrodes were dried in a vacuum oven at 120 °C overnight to remove traces of water and solvent before their transfer into an argon-filled glovebox. The anode was a lithium metal disk, and the separator was Celgard

2034. A two electrodes cell was used (Swagelok cell type), where lithium was both reference and counter electrodes. The electrolyte was 1.0 M $LiPF_6$ in propylene carbonate/ethylene carbonate/dimethyl carbonate (PC/EC/3DMC; 1:1:3 vol. %). The cells were assembled in an argon filled dried glove box. Relaxation was performed for at least 5 hours until the open circuit voltage (OCV) stabilization. Galvanostatic discharges, carried out on a VMP2-Z instrument from Biologic, were performed at room temperature by applying a constant current density of 10 mA/g with a cutoff voltage of 1 V in reduction and 4.3V in oxidation.

X-RAY Absorption Spectroscopy (XAS): X-ray absorption spectroscopy was carried out at beamline ROCK of SYNCHROTRON SOLEIL. The electrode samples were never exposed to the ambient environment during the measurement. Higher harmonics in the X-ray beam were minimized by detuning the Si(111) monochromator by 40% at the Ni K-edge (8333 eV). Transmission spectra at the Ni K-edge were collected along with a simultaneous spectrum on a reference foil of metallic Ni to assure consistent energy calibration. Energy calibration was carried out by using the first derivatives in the spectra of Ni foil. Data were analyzed and refined using Artemis software.

SYNTHESIS OF MATERIALS

$NiF_2.4H_2O$ NANOPARTICLES AND BULK MATERIAL.

The $NiF_2.4H_2O$ nanoparticles were synthesized by reverse microemulsion technique following a reported procedure[38, 50]. In a typical synthesis process, a series of $NiF_2.4H_2O$ nanoparticles (water/oil molar ratio α~0,96) were synthesized by preparing water-in-oil microemulsions of identical compositions in two separate Teflon beakers by stirring together 0.014 mol of CTAB, 0.230 mol of 2-octanol and 0.222 mol of H_2O for one hour. The water-in-oil microemulsions were named as microemulsion one (μE_1) and microemulsion two (μE_2) based on the facts that the former contained 0.002 mol of $Ni(NO_3)_2.6H_2O$ and the latter contained 0.005 mol of NH_4F. The μE_1 and μE_2 microemulsions are stirred individually for one hour and are stable after stopping the stirring, no segregation of the aqueous and organic phases has been observed After, the two microemulsions were mixed by pouring down very slowly μE_1 into μE_2.. After mixing the two microemulsions, the whole reaction mixture was stirred, at room temperature, for another 15 min (sample "1"), 30 min (sample "2") and 60 min (sample "3"). The green colored precipitate obtained in the bottom of the reaction beaker was separated from the supernatant by centrifuging at 4000 revolutions per minute (rpm) for 30 minutes. To ensure complete removal of the unutilized surfactant, oil, water and any other contamination(s), the resulting green powder was washed subsequently with 10 mL of ethanol and distilled water followed by centrifugation at 4000 rpm for 10 minutes. The washing process was repeated ten times. The thoroughly washed green powder was dried at room temperature for 24 hours.

Another series of $NiF_2.4H_2O$ nanoparticles (water/oil molar ratio α~1.21) was synthesized following the procedure described in the preceding paragraph by increasing the water contents in microemulsions (μE_1 and μE_2) to 0.278 moles, and stirring the reactions after mixing of the two microemulsions for 15 min (sample "4"), 30 min (sample "5") and 60 min (sample "6").

Attempts were also made for the synthesis of $NiF_2.4H_2O$ nanoparticles at decreased water contents (0.167 mol, water/oil molar ratio α~0.7). However, due to the instability, quite unusual, of the resulting microemulsions (μE_1 and μE_2), the syntheses were not followed. A small amount of powder was isolated in one of the cases, and characterized by different analytical techniques

(XRD, FTIR, Raman, TEM and SEM data are given in Figure S1(a-f) in the supplementary information (SI)). Because, microemulsions of this series were not stable, these samples will not be discussed here. Generally the microemulsions are stable over a long range of water contents, which is not the case here. The use of any suitable co-surfactant, which allows to favorably dispersing the water by decreasing the interfacial tension, would enhance stability of the microemulsion[51].

Bulk $NiF_2.4H_2O$, labeled “bulk-1”, was synthesized by a classical reaction in water with aqueous hydrogen fluoride (HF_{aq}). Hydrated nickel chloride ($NiCl_2.6H_2O$) was added to a large excess of 48% HF_{aq} in a Teflon beaker. The reaction mixture was stirred at 50°C followed by evaporation of the excess HF_{aq} by extractor. The resulting green colored $NiF_2.4H_2O$ powder was dried at room temperature under fume hood and then stored in a clean vial. A complete summary of the synthesis protocol and parameters of the samples “1”-“6” (Scheme S1 and Table S1) are presented in Supporting Information (SI).

ANHYDROUS NiF_2 NANOPARTICLES AND BULK MATERIAL

The NiF_2 nanoparticles were synthesized in a two steps process by the dehydration of $NiF_2.4H_2O$ nanoparticles. In first step, a weighed amount of hydrated nickel fluoride powder ($NiF_2.4H_2O$ nanoparticles) was placed in a nickel boat which was then inserted into the chamber of Buchi Incorporation vacuum drying system. Upon achieving the target vacuum, the chamber was heated to 100°C and maintained for one hour. Afterwards, the temperature of the chamber was raised to 250°C and maintained for another five hours. At the end of the process the system was allowed to cool down naturally to room temperature. The color of powder turned yellow from green[52]. The purposely designed procedure was followed to get transformed $NiF_2.4H_2O$ to NiF_2 successfully while retaining the basic shapes and structures of the self-assembled nanoarchitectures synthesized by microemulsion. The temperature regimes for the separately manipulated steps were decided following the TGA curve of bulk and $NiF_2.4H_2O$ nanoparticles. TGA curve of bulk sample is given in Figure S2 which shows a main weight loss between 100°C and 300°C with a maximum at approximately 163.3°C. At this temperature, $NiF_2.0.3H_2O$ is achieved and the remaining 0.30 H_2O molecules per formula unit are released in the steady and continuous step up to 340°C.

In a second step, the nickel boat containing the vacuum dried and/or partially dehydrated powder of the sample was inserted into the chamber of fluorination furnace. The furnace was purged with dry N_2 gas for two hours and then heated at the rate of 5°C/min to reach the target temperature of 350°C. When the temperature reached 250°C, N_2 supply was disconnected and pure F_2 gas was allowed to enter the furnace chamber. The dynamic fluorination was continued at 350°C for five hours. Afterwards, the F_2 supply was stopped and N_2 was opened into the chamber. The chamber was allowed to cool down to room temperature naturally under gaseous N_2 environment. Finally, dehydrated nickel fluoride (NiF_2) powder was retrieved into a clean vial. The same procedure was repeated for the transformation of all $NiF_2.4H_2O$ samples “1”, “2”, “3”, “4”, “5” and “6” to NiF_2 samples labeled “1-1”, “2-2”, “3-3”, “4-4”, “5-5” and “6-6”, respectively. The cartoon drawing of the furnace used for the dehydration of hydrated nickel fluorides is given in Figure S3 and the relevant dehydration parameters are summarized in Table S2.

The procedure for synthesis of bulk dehydrated nickel fluoride (NiF_2), labeled “bulk-2”, is exactly the same as was adopted for the preparation of dehydrated nano-NiF_2 from hydrated nickel fluorides nanoparticles ($NiF_2.4H_2O$). The synthesis parameters and samples labels of all the obtained samples are summarized in Table 1.

Table 1. Summary of the main synthesis parameters and samples labels of $NiF_2.4H_2O$ / NiF_2 nanoparticles and bulk material.

Sample	**H_2O/Oil α (mole/mole)**	**Time (Min)**	**Sample**	**Heating under Vacuum Temp./Time (°C/H)**	**Fluorination Temp./Time (°C/H)**
"1"	0.96	15	**"1-1"**	250/5	350/5
"2"	0.96	30	**"2-2"**	250/5	350/5
"3"	0.96	60	**"3-3"**	250/5	350/5
"4"	1.21	15	**"4-4"**	250/5	350/5
"5"	1.21	30	**"5-5"**	250/5	350/5
"6"	1.21	60	**"6-6"**	250/5	350/5
"Bulk-1"	--	--	**"Bulk-2"**	250/5	350/5

RESULTS AND DISCUSSION

$NIF_2.4H_2O$ NANOPARTICLES AND THEIR SELF-ASSEMBLIES.

The $NiF_2.4H_2O$ nanoparticles and their self-assemblies were prepared at two different values of ω (molar water/surfactant ratio) i.e., 16.18 and 20.23 following the reported procedures[38, 50]. Simultaneously, the water/oil molar ratio is changed from $\alpha<1$(~0.96) to $\alpha>1$ (~1.21) for the $NiF_2.4H_2O$ nanoparticle series prepared at $\omega = 16.2$ and $\omega = 20.2$, respectively. As presented in Table S1, samples were obtained by varying the ω and reaction time from 15 min (sample "1") to 30 min (sample "2") to 60 min (sample "3").

Powder X-Rays Diffraction (XRD) patterns of all the samples (“1” to “6” and “Bulk-1”) are presented in Figure 1-a. The XRD patterns give narrow and intense peaks at 2θ positions matching with the powder diffraction files (PDF) of $NiF_2.4H_2O$ ([00-025-0579] and [04-008-9585]) in ICDD (International Center for Diffraction Data) database. The search and match results confirm the orthorhombic crystal system with $P2_1ab$ space group of $NiF_2.4H_2O$ crystals. The intense and narrow peaks indicate the formation of well grown crystallites of $NiF_2.4H_2O$ in all the samples. The crystallite sizes were estimated by Scherrer’s approximation (Eq. 1), and presented in Table 2. As evident from Table 2, the crystallite size increases slightly with increasing ω and the reaction time. This was anticipated and in accordance to the previous reports about the effect of water contents over the crystallite and/or grain size[53], but in our case the effect is smaller. In fact, the increase in water content is responsible for increasing the droplet size and thus, decreasing its rigidity[54]. The decrease in droplet rigidity enhances the exchange rate (diffusion rate) which is responsible for fast growths of crystals[55]. However, certain other factors could also influence particle nucleation and growth, among them inter-micellar interactions and dynamic behavior, phase behavior (e.g. solubility), average occupancy of the water pool by the reactant (i.e., precursor concentration) can be cited. The use of cationic CTAB as surfactant can especially influence the packing parameter and the interfacial rheology, due to interaction with precursor salts. In our case, while some parameters may lead to faster kinetics, some others favor slower kinetics. As a global result, the size of the primary particles remains nearly unaffected [56-57]. It is pertinent to mention here that though the increase in crystallite size with increasing water contents is slight but the overall crystallite size is quite very small compared to that reported previously in case of BaF_2 by the very same water-in-oil microemulsion system[38].

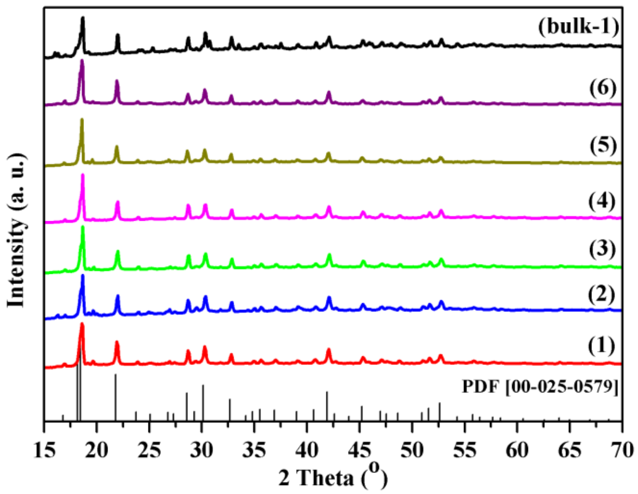
(bulk-1)
(6)
(5)
(4)
(3)
(2)
(1)
PDF [00-025-0579]
Intensity (a. u.)
15 20 25 30 35 40 45 50 55 60 65 70
2 Theta (°)

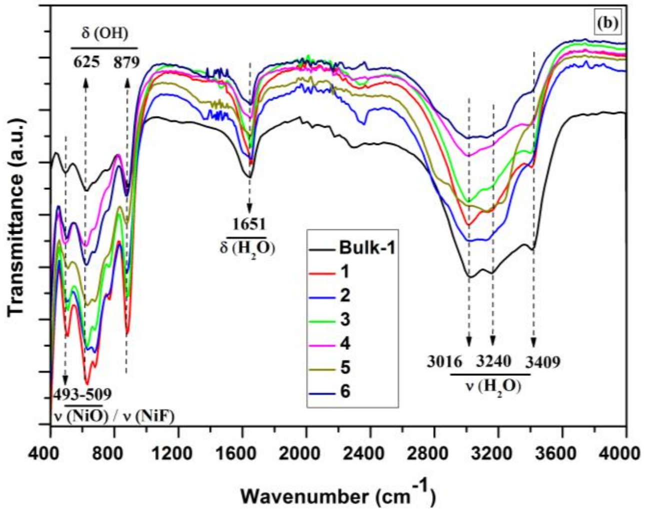
(b)
δ (OH)
625
879
1651
δ (H_2O)
Bulk-1
1
2
3
4
5
6
3016
3240
3409
ν (H_2O)
493-509
ν (NiO) / ν (NiF)
Transmittance (a.u.)
400 800 1200 1600 2000 2400 2800 3200 3600 4000
Wavenumber (cm^{-1})

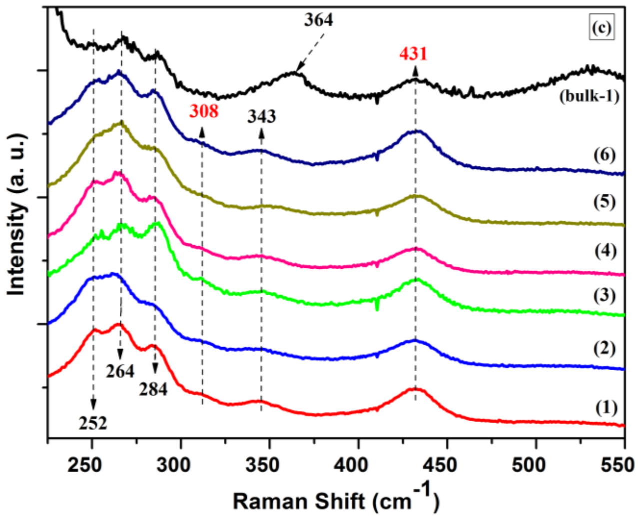
(c)
364
431
308
343
(bulk-1)
(6)
(5)
(4)
(3)
(2)
(1)
264
284
252
Intensity (a. u.)
250 300 350 400 450 500 550
Raman Shift (cm^{-1})

Figure 1. (a) XRD patterns, (b) FTIR and (c) Raman spectra of bulk ("bulk-1) and nano-$NiF_2.4H_2O$ samples ("1" to "6") synthesized respectively by the reaction with HF_{aq}, and water-in-oil microemulsion technique under varying ω and α ratios and reaction time.

The obtained $NiF_2.4H_2O$ nanoparticles are confirmed by FTIR and Raman analyses. FTIR spectra of $NiF_2.4H_2O$ bulk and nanoparticles are presented in Figure 1-b. The FTIR spectra of the $NiF_2.4H_2O$ nanoparticles are in good agreement with the IR spectrum of bulk $NiF_2.4H_2O$ embedded in Figure 1-b, and also with the previously reported[58]. The mid FTIR spectra of $NiF_2.4H_2O$ bulk and nanoparticles give stretching and bending peaks for O–H of H_2O in the range of 3409 – 3016 cm^{-1} and 1651 cm^{-1}, respectively[59-61]. The peaks which are absent in the FTIR spectrum of "bulk-1" and appear at 2816 cm^{-1}, 1466 cm^{-1} and 1396 cm^{-1} in the FTIR spectra of samples "1"-"6" are corresponded to the adsorbed surfactant molecules. The fewer than actual peaks of pure CTAB is the indication of the fact that the surfactant molecules are in strong interaction with $NiF_2.4H_2O$ nanoparticles[62]. The weak peak around 2330 cm^{-1} in FTIR spectra of all the samples is ascribed to the combination of bending and rocking vibrations of H_2O[58]. A number of peaks appear in the FTIR spectra of bulk as well as nanoparticles in the 900 cm^{-1} to 400 cm^{-1} region. The two peaks of medium intensity at 879 cm^{-1} and 764 cm^{-1} are due to the rocking while the other two peaks of comparatively weak intensity at 679 cm^{-1} and 632 cm^{-1} correspond to the wagging vibrations of H_2O [58]. The peak around 509 cm^{-1} is assigned to the Ni-F stretching vibration[58]. The IR spectra of metal fluoride nanoparticles prepared from nitrate salts can show significant peaks for NO_3^- stretching vibrations around 1384 cm^{-1}. However, the IR spectra of all the samples do not contain peaks of NO_3^-. The samples were also analyzed by Raman spectroscopy in the range of 600 cm^{-1} – 300 cm^{-1} at room temperature under air. The Raman spectra (Figure 1-c) of all the samples correspond to each other. The peaks at 431 cm^{-1}

and 308 cm^{-1} corresponds to A_{1g} and E_g vibration modes of NiF_2, respectively[63]. The rest of the peaks are due to the different vibration modes of Ni – O bond and H_2O, and symmetric stretching mode of hydrogen bond[64-65].

Table 2. Crystallite and individual particle sizes of $NiF_2.4H_2O$ and NiF_2 nanoparticles and their bulk counterparts determined by XRD and TEM respectively.

Sample	**Crystallite/Individual Particle size**		**Sample**	**Crystallite/Individual Particle size**	
	XRD (nm)	**TEM (nm)**		**XRD (nm)**	**TEM (nm)**
“1”	15.2	15.7±4.3	**“1-1”**	13.4±0.7	24.0±8.0
“2”	16.8	17.3±4.1	**“2-2”**	14.2±2.0	26.0±2.5
“3”	17.9	19.2±8.4	**“3-3”**	14.3±2.4	26.8±4.6
“4”	18.3	18.9±6.4	**“4-4”**	14.8±2.2	31.4±3.2
“5”	20.8	20.1±9.4	**“5-5”**	14.2±2.0	13.6±3.2
“6”	24.4	23.0±7.1	**“6-6”**	15.7±2.9	29.9±4.6
“Bulk-1”	48.1	>250(i)	**“Bulk2”**	37.2±22.1	>250

(i) irregular shaped particles spread over a wide range of size

SEM images of samples “1” to “3” and “4” to “6” are presented in Figure 2 and Figure 3, respectively. SEM images of sample “1” ($\omega = 16.18$, $\alpha < 1$ and reaction time of 15 min) show predominant and larger structures having almond-like shapes, and less frequent and smaller truncated bi-pyramidal structures (Figure 2-a, b). The almond-like structure looks anisotropic having average length and width in order of 6-7 μm and 3-4 μm, respectively. However, the truncated bi-pyramids seem isotropic having average size of 5-6 μm. The bi-pyramids seem to be formed as a result of auto-assembling of smaller structures perhaps cubes (Figure 2b inset). Furthermore, the truncated faces of the bi-pyramids are rough while the isosceles trapezoid facets are smooth. This could be due to the slow growth rate along z-axis direction (vertical) and rapid growth rate along x- and y-axis directions (horizontal). The morphologies of sample “2” (Figure 2-c, d) and “3” (Figure 2-e, f) are not too different than that of sample “1”. The same larger almond shape and smaller truncated bi-pyramidal structures are also seen in the SEM images of sample “2” and “3”. However, as the reaction time – at same ω and α ratios – increases from 15 min (sample “1”) to 60 min (sample “3”), the size of almond shaped structure increases slightly from the order of 6-7 μm to 7-7.5 μm. The magnified SEM images of sample “2” (Figure 2-d) and “3” (Figure 2-f) show a cascade auto-organization of the cubes into truncated bi-pyramids which further auto-organize into almond shaped macrostructures.

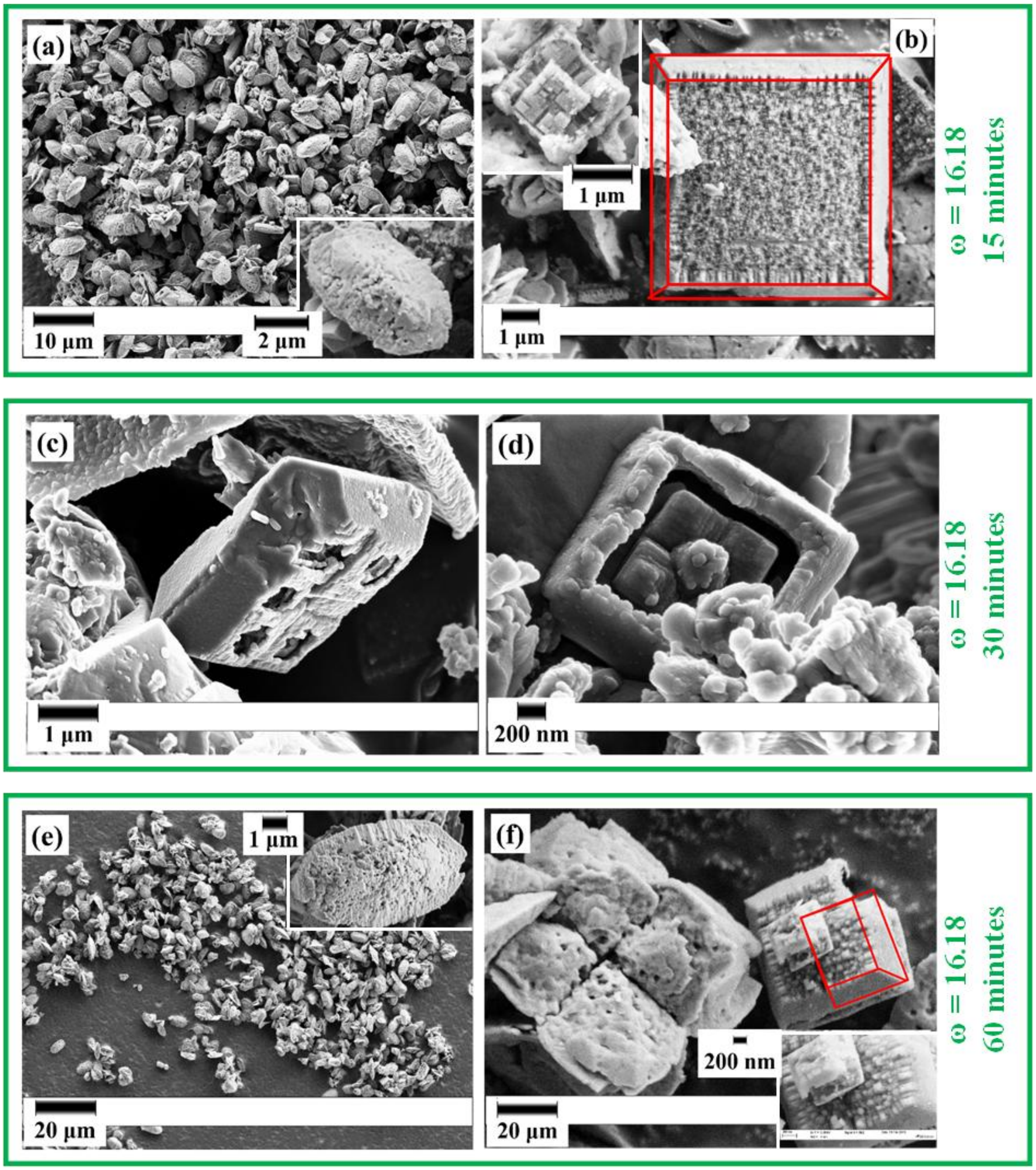

Figure 2. SEM images showing almond-like structures of samples “1” (a) and “3” (e), truncated bipyramids of samples “1” (b), “2” (c) and “3” (f), incomplete pyramidal wall encompassing auto-organized small pyramids of sample “2” (d), and auto-organized truncated bipyramids into superstructure of sample “3” (f); insets in (a) and (e) show magnified almond-like structures of samples “1” and “3”, respectively

Upon increasing the ω from 16.18 and $\alpha < 1$ (samples "1" to "3") to $\omega = 20.23$ and $\alpha > 1$ (samples "4" to "6"), variations in morphologies of the resulting $NiF_2.4H_2O$ nanomaterials are observed in the SEM images (Figure 3-a – f). As shown in Figure 3-a, the SEM image of sample "4" ($\omega = 20.23$, $\alpha > 1$ and reaction time of 15 min) shows truncated bi-pyramids which are highly agglomerated through the isosceles facets. The average size of the truncated bi-pyramids is in the order of 8-8.5 μm. The rupture running along the center of the truncated bi-pyramidal shapes indicates that the structures are not fully developed to form well defined almond-like structures (Figure 3-b and 3-b inset). However, the SEM images of samples "5" (Figure 3-c) and "6" (Figure 3-e) show the very almond shaped structures which upon magnification resembling boats covered on both the sides by vertically standing truncated bi-pyramids. The sizes of the almond-like structures formed in sample "5" and "6" are in the order of 19-20 μm and 22-23 μm, respectively, and are far larger than those of samples "1" to "3". The surfaces of almonds-like assemblies are covered on both the sides by truncated bi-pyramidal structures as shown in Figure 3-d (sample "5") and 3-f (sample "6"). In fact, the almond-like super-structures are formed as a result of horizontal auto organization of truncated bi-pyramids, and after attaining a threshold size of the almond-like structures, the horizontal growth stops on the expense of a new growth initiation on the high energy truncated facets of almonds. The truncated bi-pyramidal structures are aligned through the truncated facets owing to interdigitation of surfactant molecules[29].

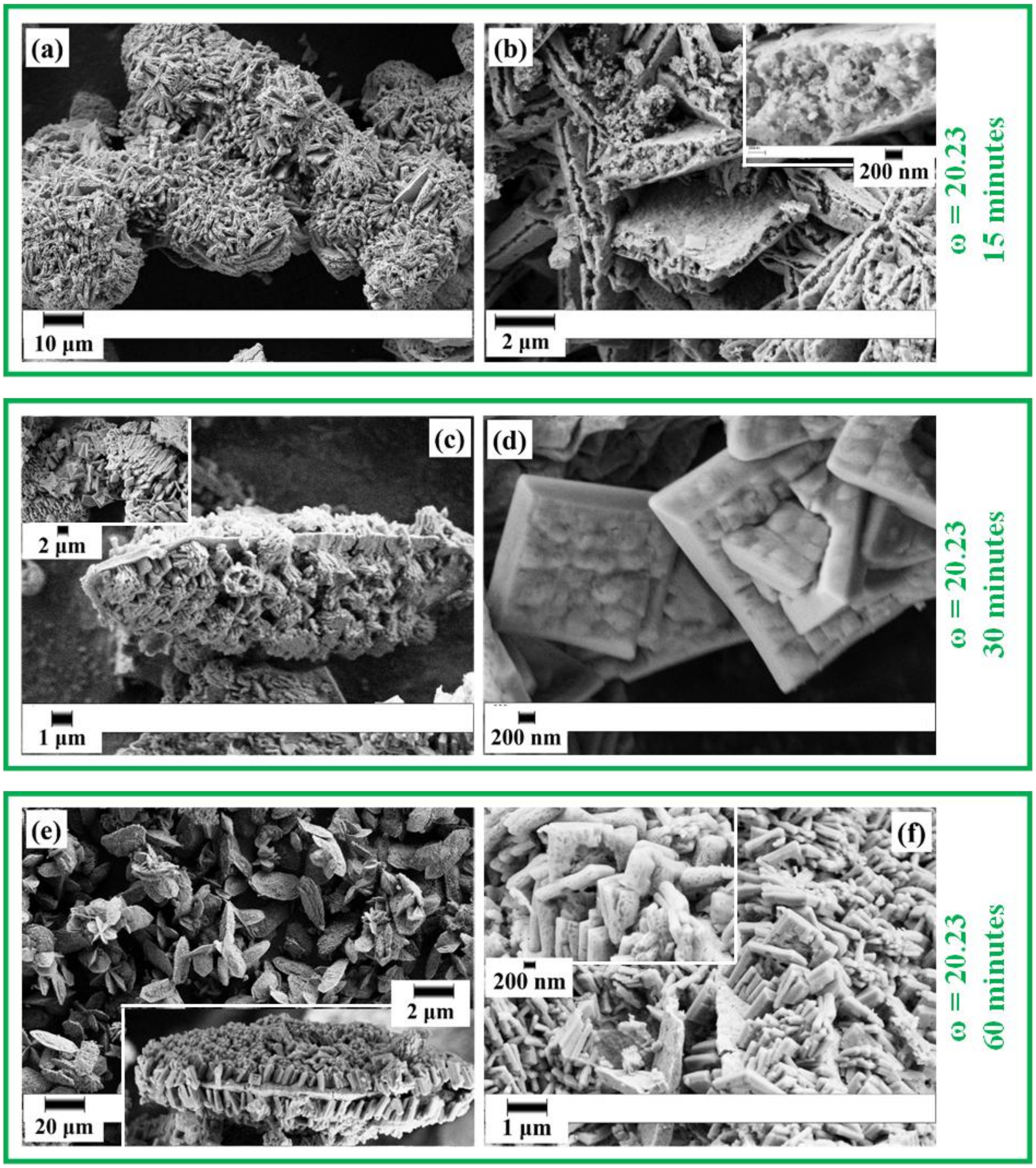

Figure 3. SEM images showing agglomerated truncated bi-pyramids of sample “4” (a), large almonds super-structures covered with sub-structures of samples “5” (c) and “6” (e), underdeveloped truncated bi-pyramids of samples “4” (b) and well organized through truncated facets truncated bi-pyramids of samples “5” (d) and “6” (f); inset in (b) shows magnification of rupture in truncated bi-pyramids of sample “4”, in (e) magnification of a super-structure of

sample “6” and in (f) magnification of auto-organized through truncated facets truncated bipyramids of sample “6”.

TEM images of samples “1” to “3” ($\omega = 16.18$, $\alpha < 1$) are presented in Figures 4. Figure 4-a – TEM image of sample “1” – shows an elongated hexagonal super-structure (length = 3.37 μm and width = 1.94 μm). A small square ¼ the size of hexagon is also seen. The square structure has a cleavage along the diagonal, and seems to be formed of single layer of nanoparticles in the center while a second layer growth is observed on the edges. It seems that the cleaved square particle is the result of auto-assemblage of nanoparticles. This hypothesis of nanoparticles auto-assemblage into square is further augmented by the larger magnification TEM image (Figure 4-b) showing self-assembled nanoparticles in horizontal layers which are packed successively into a cuboid structure (Figure 4-b inset). In fact, the cuboids and the hexagons are not two different structures formed, but the hexagonal architecture is the result of further auto-organization of the cuboids. In fact, these structures can be assimilated respectively to the almond-like (hexagons) and truncated bi-pyramid (cuboids) structures observed in the SEM pictures. TEM images of sample “2” ($NiF_2.4H_2O$ synthesized at $\omega = 16.18$, $\alpha < 1$ and reaction time of 30 min) and “3” ($NiF_2.4H_2O$ synthesized at $\omega = 16.18$, $\alpha < 1$ and reaction time of 60 min) in Figure 4-c and Figure 4-e, respectively, also show similar structures i.e. larger hexagonal and their approximately ¼ square shaped as were observed in TEM images of sample “1”. The average size of hexagons and cuboids are increasing upon increasing the reaction time at the same ω and α ratio. This is in good agreement with the sizes evolution observed in the SEM images (Figure 2) for the almond-like and truncated bi-pyramid structures. For example the average lengths and widths of hexagons of sample “2” (11.67 μm and 5.36 μm) and “3” (13.70 μm and 7.47μm) are longer than that of sample “1” (3.37 μm and 1.94 μm). Similarly the average size of squire measured for sample “2” (2.62 μm) and “3” (3.18 μm) are larger than sample “1” (1.25 μm). Furthermore, the relatively compact cuboids and hexagons shown in TEM images of sample “2” and “3” suggest that the auto-assemblage efficiency of nanoparticles increases with increasing reaction time. The self-assembling of nanoparticles in sample “2” and “3” seems to have followed the same mechanism as was observed in sample “1”. The successive (vertical) growth indicated in Figure 4-d (inset) and 4-f (inset) further support the layer by layer growth mechanisms in sample “2” and sample “3”, respectively. The individual particle size increases slightly as a function of increasing reaction time from 15 min to 30 to 60 min (Table 1).

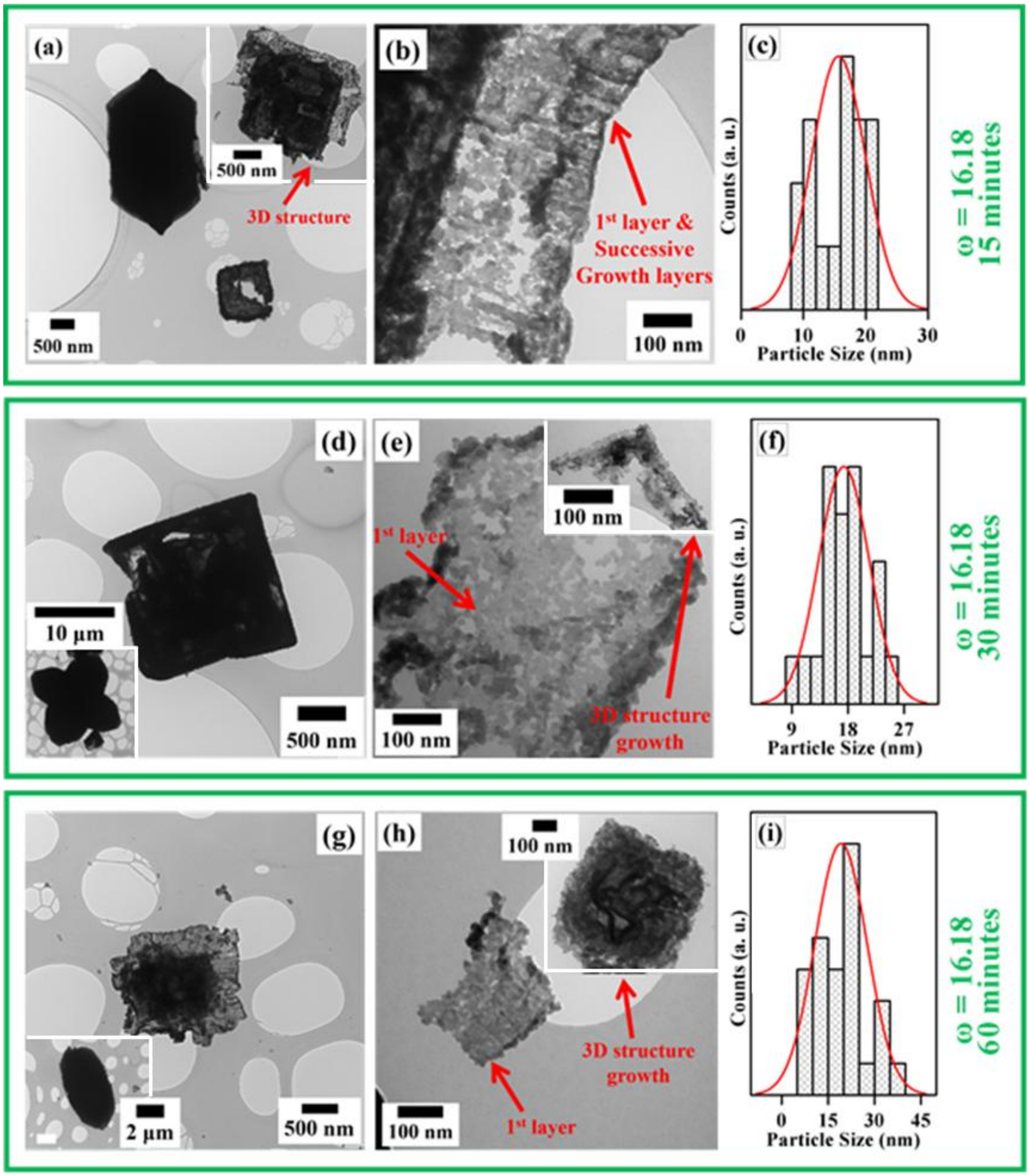

Figure 4. TEM images of samples “1” (a, b), “2” (d, e), and “3” (g, h); the histograms (c), (f) and (i) are the particle size distributions of the samples “1”, “2”, and “3” respectively; insets in (a), (e), and (h) are the layer by layer formed 3D structures of samples “1”, “2”, and “3”, respectively. Insets in (d) and (g) are almond-like structures observed in samples “2” and “3” respectively.

TEM images of samples “4” to “6” synthesized by microemulsion having larger water contents (ω = 20.23 and α >1) are given in Figure 5. The increase in ω from 16.18 to 20.23 resulted in formation of distorted-hollow-spherical $NiF_2.4H_2O$ structures as primary auto-assemblies of individual nanoparticles, a phenomenon which was not observed in case of sample “1” – “3”. The deformation in shapes of hollow spheres could be correlated to their coalescence and thus formation of larger irregular hollow nanostructures. The coalescence increases with increasing reaction time as is evident from the TEM images in Figure 5-a – e. The increase in ω from 16.18 to 20.23 resulted in different first self-assemblies. However, the consequent (second) self-assemblies of the hollow nanostructures followed the auto-organization mechanism observed in case of sample “1” to “3”. The deformed hollow nanostructures self-assemble into layers which packed successively to give 3D architectures. The TEM images given in Figure 5-b and 5-d of the samples “4” and “5”, respectively, show partial self-assemblies. However, cuboid structure is observed in TEM image of sample “6” (Figure 5-f). Furthermore, the existence of hexagon like shape in TEM image of sample “6” (Figure 5-f inset) indicates that the cuboids further auto-organize as was the case in samples “1” to “3”. As indicated in the case of samples "1"-"3", the hexagons and cuboids observed here correspond respectively to the almond-like and truncated bi-pyramids structures observed in the SEM images (Figure. 3). In fact, the hollow-spherical nanostructures auto-assemble in case of samples “4” to “6” but the packing efficiencies are not high enough to resist their disorganization induced by the sonication performed during sample preparation for TEM analysis. On the other hand, nanoparticles in the first assemblies (distorted hollow spheres) are coherent, and thus remain intact as shells of hollow spheres after sonication. The $NiF_2.4H_2O$ nanoparticle size estimation from the TEM images of samples “4” to “6” is difficult due to stronger aggregation of the particles than for samples “1” to “3”. However, the particle size estimated from the thickness of the walls of the hollow spheres of sample “4” to “6” indicates that the size of individual nanoparticles increases slightly but consistently with the increasing ω and the reaction time. For example, as also shown in Table 2, the average nanoparticle sizes estimated from TEM images for the samples “1” to “3” and“4” to“6” are 15.7±4.3 nm to 19.2±8.4 nm, and 18.9±6.4 nm to 23.0±7.1 nm, respectively.

The bulk material synthesized is obtained with irregular shape and non-uniform big chunk shown by the TEM images (supplementary Figure S4).

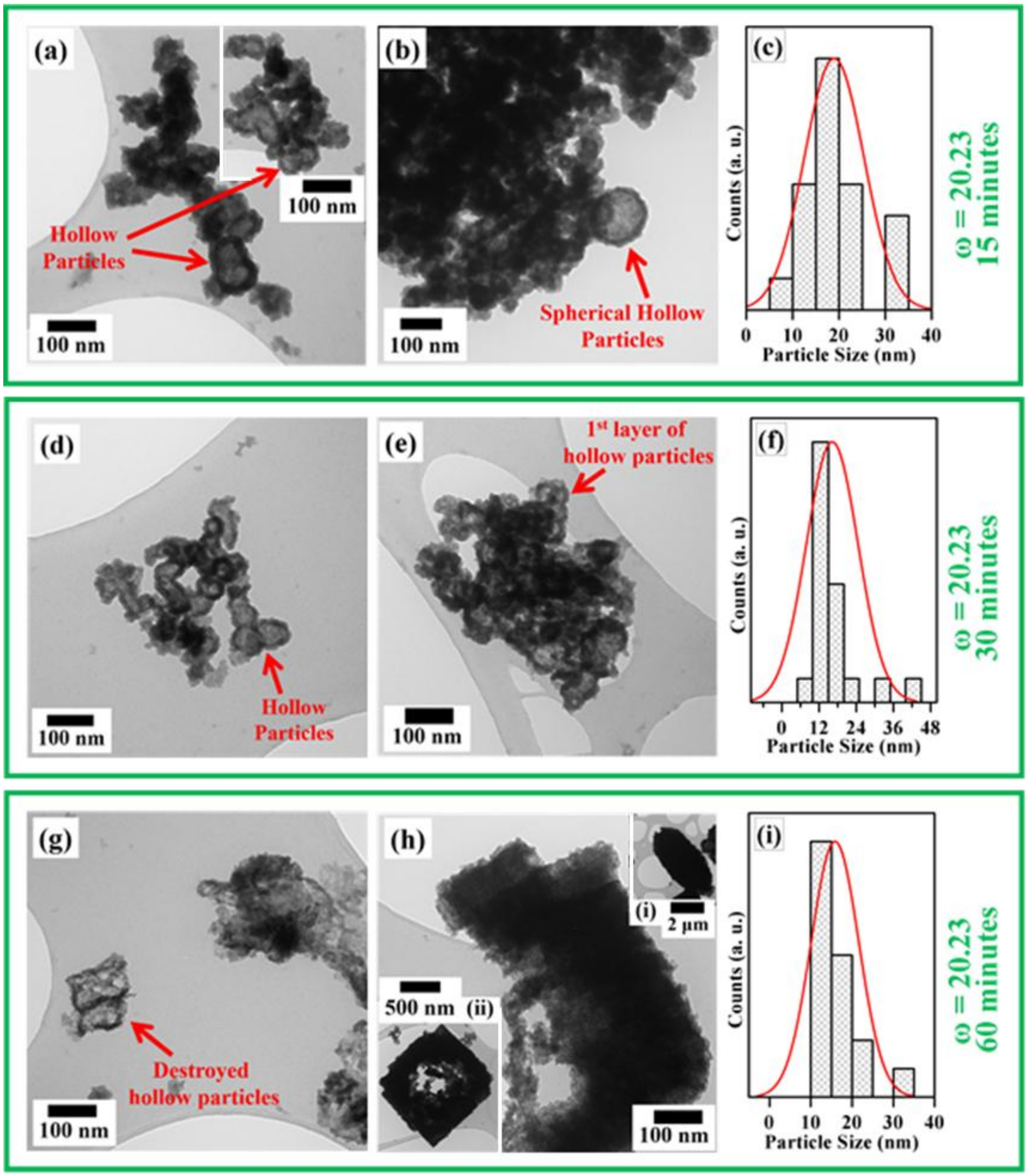

Figure 5. TEM images of samples “4” (a, b), “5” (d, e), and “6” (g, h); inset in (a) shows the successive layers of deshaped-hollow-spheres; insets in (h) show the cuboid and almond-like structures. The histograms (c), (f) and (i) are the particle size distributions of the samples “1”, “2”, and “3” respectively.

An auto-organization mechanism is proposed in Figure 6. The formation of $NiF_2.4H_2O$ nanoparticles in the two series (samples “1” to “3” and “4” to “6”) is slightly different, chiefly owing to the difference in ω, α ratio and reaction time. At $\omega = 16.18$ and $\alpha <1$, the water droplet is smaller, and thus, irrespective of the reaction time, the diffusion of reactants lead to the formation of dense nanoparticle suspended in the water pool. On the other hand, upon increasing the ω to 20.23 and $\alpha >1$, the size of micelle increases, and thus, as the reaction occurs at the interface, hollow spheres form at lower reaction time owing to the auto-organization of the nanoparticles into a shell encompassing the water pool (droplet). However, as the reaction time increases, the inward growth of the nanostructure in the micelle leads to the formation of thick wall hollow-spheres, and finally dense nanoparticles of larger size. The dense nanoparticles (samples “1” to “3”) and the hollow spheres (samples “4” to “6”) self-assemble into cuboids in a concentric growth. The cuboids further self-assemble into 2D superlattices suggesting a faster growth in XY plane (horizontal) than in the z-axis direction (vertical). Owing to the fast growth in horizontal directions, the superlattices turned into truncated bi-pyramidal structures which eventually auto-organize themselves into almond-like super-structures. The auto-organization of the nanoparticles and then of the different structures like cuboids or truncated bi-pyramids is in fact controlled by the surfactants molecules on their surfaces and faces. As was observed previously[29], the surfactant molecules on the surface of nanoparticles or on the facets of bigger structures act as anchorage sites by interdigitating their alkyl chain, and consequently, align the structures into ordered assemblies. This phenomenon is more evident from the SEM images of sample “5” (Figure 3-c & d) and “6” (Figure 3-e & f) in which the truncated bi-pyramidal super-structures are parallely aligned through the truncated facets. It is worth noting that the individual nanoparticles average size is not significantly related to the time parameter, but is rather is due to the water/oil ratio (α). Conversely, the time parameter drives the super-structure sizes. In conclusion, excepted slight differences about the sizes of the individual nanoparticles and that the sizes of super-structures depend of the reaction time, there is no crucial differences between the obtained self-assembled nanostructures.

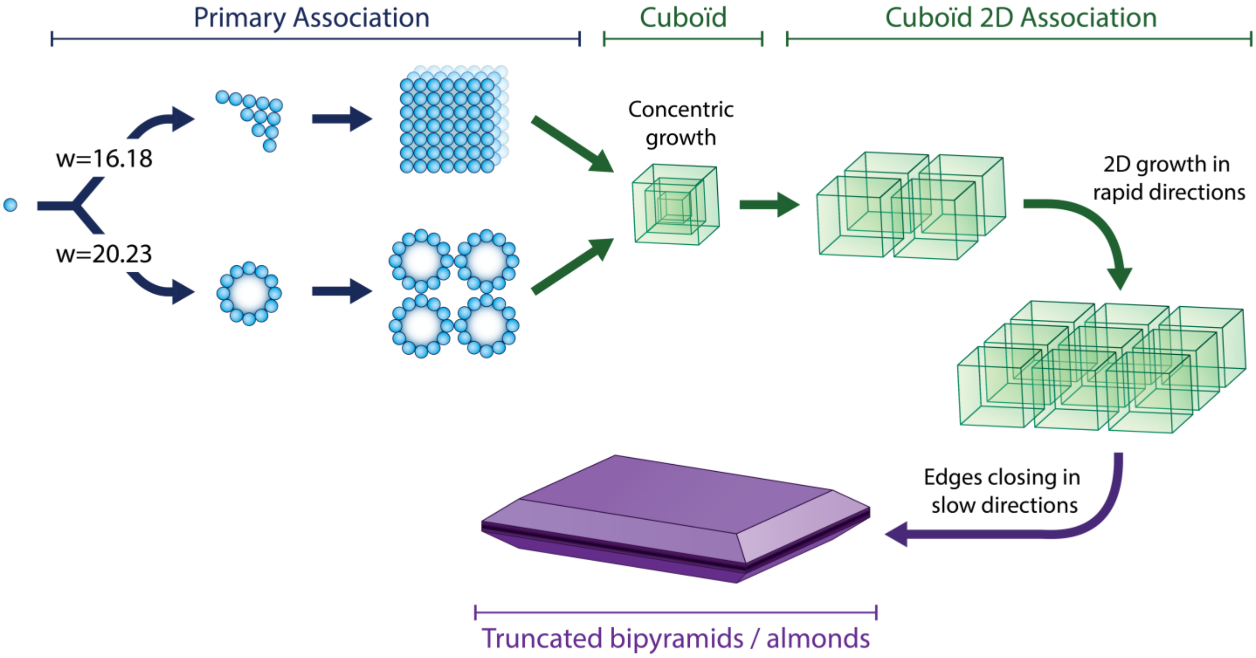

Figure 6. Schematic of cascade auto-organization process of nanoparticles/spheres into self-assembled super-structures

NiF_2 NANOPARTICLES, THEIR SELF-ASSEMBLIES AND THEIR PROPERTIES

Conversion under F_2:

NiF_2 nanostructures were prepared from $NiF_2.4H_2O$ nanoparticles self-assemblies by a deliberated two-step process. The carefully designed step by step heating process was followed in order to eliminate completely the crystallization water molecules from the lattice without damaging the self-assembled super structures. The simple vacuum drying is unable to deliver completely anhydrous crystalline NiF_2.

The XRD pattern of a vacuum dried sample shows no clear peaks except a couple of broad humps (Figure 7-i). This indicates that the yellow powder[52] obtained at the end of first step is amorphous. The amorphosity of powders is also evident from the Raman scattering spectrum which shows a broad peak around 400 cm^{-1} (Figure 7-iii). This indicates that upon removal of water, the lattice structure collapses. However, the removal of water is not complete, and this is evident from the IR spectrum which is comparable to that of precursor. As shown in Figure 7-ii, the FTIR spectrum gives broad peaks around 3220 cm^{-1} and 1612 cm^{-1} for O – H stretching and bending vibrations, respectively, and at 679 cm^{-1} for H_2O libration mode. This indicates that the dehydration of $NiF_2.4H_2O$ is incomplete at the end of first step. Nonetheless, TEM images show that the self-assemblies of nanoparticles are intact (supplementary Figure S5).

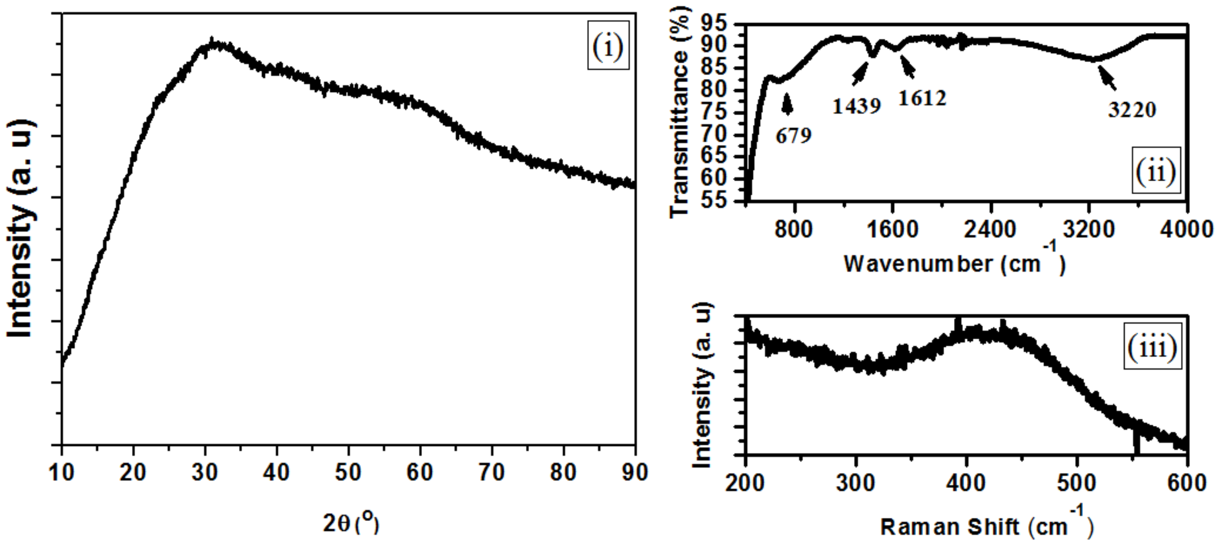

Figure 7. X-rays diffractogram (i), FTIR (ii) and Raman (iii) spectra of vacuum dehydrated $NiF_2.4H_2O$ nanoparticles (sample 5) at 100°C for 1 hour followed by at 250°C for 5 hours.

The resulting NiF_2 nanoparticles obtained at the end of the second step are crystalline as evidenced by the diffractograms presented in Figure 8-a. The peaks of all the samples ("1-1" to "6-6") are indexed as NiF_2 in tetragonal structure having P42/mnm space group by matching with powder diffraction files (PDF) number [01-74-0917] and [00-24-0791][66]. The NiF_2 nanoparticles in all the samples consist of single phase as the XRD patterns show no peaks other than those of tetragonal NiF_2. The average crystallite size was determined by Scherrer formula given in Eq. 1 ($d = 0.94\lambda/\beta\cos\theta$)[67]. As shown in Table 2, the average crystallite size slightly increases as the time and the water contents of the reaction, employed for the synthesis of precursors, $NiF_2.4H_2O$, increases. It indicates that the crystallite size trend observed in hydrated $NiF_2.4H_2O$ nanoparticles is preserved after transformation to dehydrated NiF_2 nanoparticles. However, by comparing the crystallite size data in Table 2 of the hydrated and dehydrated NiF_2, respectively, the overall grain size is smaller in the dehydrated NiF_2 than the hydrated $NiF_2.4H_2O$ nanoparticles. This could be attributed to the shrinkage of lattice after removal of water.

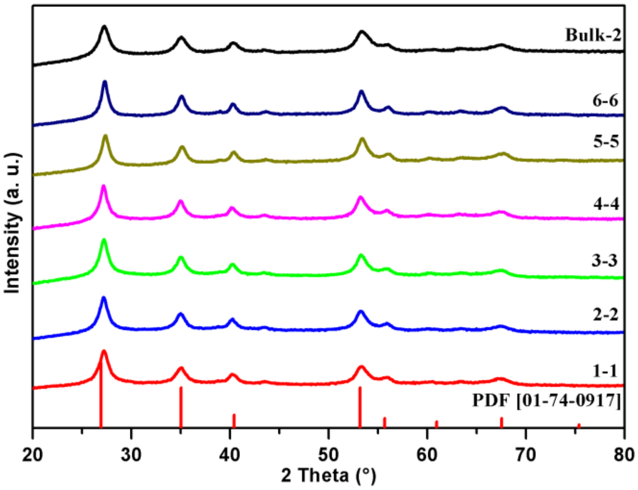
Bulk-2
6-6
5-5
4-4
3-3
2-2
1-1
PDF [01-74-0917]
Intensity (a. u.)
20
30
40
50
60
70
80
2 Theta (°)

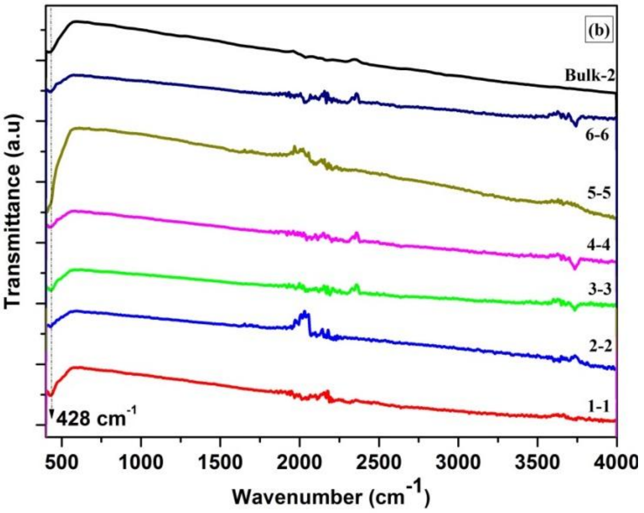
(b)
Bulk-2
6-6
5-5
4-4
3-3
2-2
1-1
428 cm⁻¹
Transmittance (a.u)
500
1000
1500
2000
2500
3000
3500
4000
Wavenumber (cm⁻¹)

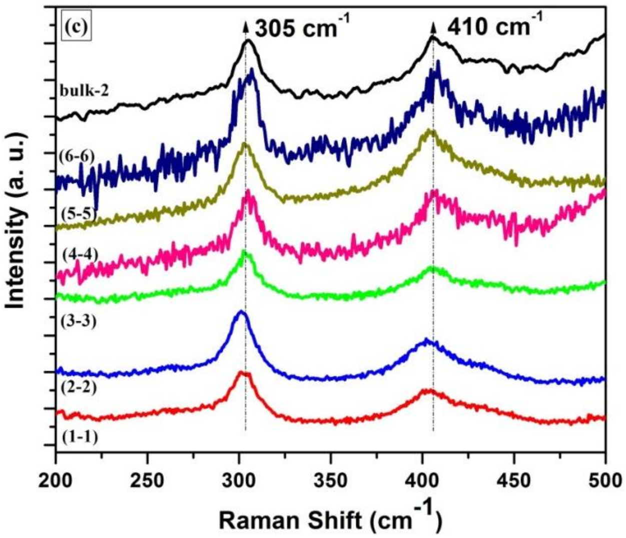
(c)
305 cm⁻¹
410 cm⁻¹
bulk-2
(6-6)
(5-5)
(4-4)
(3-3)
(2-2)
(1-1)
Intensity (a. u.)
200
250
300
350
400
450
500
Raman Shift (cm⁻¹)

Figure 8. (a) Diffractograms, (b) FTIR, and (c) Raman spectra of NiF_2 samples “1-1”, “2-2”, “3-3”, “4-4”, “5-5” and “6-6” synthesized in a two-step process by the dehydration of $NiF_2.4H_2O$ nanoparticles samples “1”, “2”, “3”, “4”, “5” and “6” respectively, and bulk NiF_2 (“Bulk-2”) prepared from bulk $NiF_2.4H_2O$ (“Bulk-1”).

The typical mid FTIR spectra of samples “1-1” – “6-6” and bulk NiF_2 (“Bulk-2”) are presented in Figure 8-b. The IR spectra show that all the samples absorb moderately in the range of 450 cm^{-1} – 410 cm^{-1}. The single peak in this range corresponds to the NiF_2 vibration[68], and shifts to higher wave numbers due to nanostructuration in the spectra of NiF_2 nanoparticles corresponding to the bulk. Apart from this peak, no other peak has been observed as shown in Figure 8-b. The complete absence of peaks other than the one mentioned indicates that the H_2O molecules are completely removed under the given synthesis parameters.

Raman scattering spectra of NiF_2 nanoparticles (samples “1-1” to “6-6”) is in accordance with FTIR spectra, confirming efficient removal of H_2O molecules. Raman spectra of NiF_2 nanoparticles (samples “1-1” to “6-6”) is presented in Figure 8-c which gives only two peaks in the range of 500 cm^{-1} – 200 cm^{-1}, and all the bands observed in the Raman spectra of precursors (Figure 1-c) due to H_2O vibrations are absent. NiF_2, a rutile structure compound having space group D_{4h}^{14}, has two raman active modes in the range of 500 cm^{-1} – 200 cm^{-1} i.e., A_{1g} and E_g giving bands around 410 cm^{-1} and 305 cm^{-1}, respectively[63, 69]. Therefore, these peaks are assigned to the NiF_2 vibrations due to A_{1g} and E_g modes. A slight red shift is observed with increase in crystallite size[70].

TEM images of the progenies (samples “1-1” to “6-6”) are acquired to follow the preservation and/or retention of the self-assemblies of the precursors (samples “1” to “6”) after dehydration of $NiF_2.4H_2O$ into NiF_2. Figure 9 and Figure S6, TEM images of samples “1-1” to “6-6”, show two types of self-assembled structures i.e., a larger almond-like and a comparatively smaller cuboids as were seen in the TEM images of the precursors (Figure 2 and 3). Furthermore, the 3D layer by layer construction of the self-assemblies of precursors is also observable in the TEM images of the derivatives (samples “1-1” to “6-6”). The nanoparticles are orderly arranged in horizontal layers which are subsequently packed/stacked giving cubic structures. The cuboids are further auto-organized giving truncated bi-pyramids and almond-like super-structures. The TEM images clarify the fact that the superlattices are the result of cascade auto-organization process. The sizes of the individual spherical-shaped nanoparticles observed on TEM images are bigger than the crystallites sizes determined by XRD analysis (Table 2). This suggests that, after thermal treatment under F_2, the obtained individual nanoparticles are polycrystalline. The moderate temperature (350°C) could have caused a slight sintering between a few neighboring crystallites.

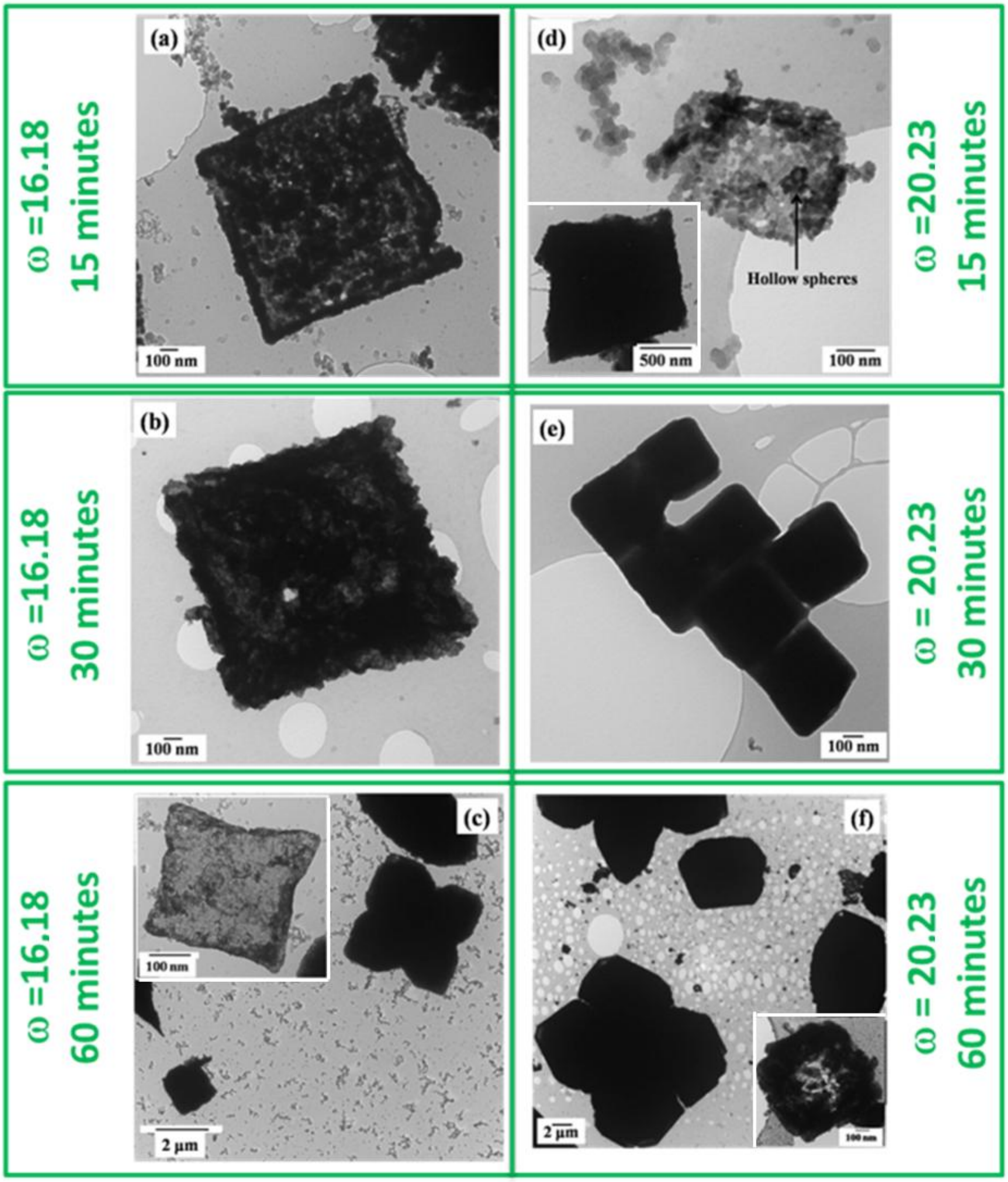

Figure 9. TEM images of samples “1-1” (a), “2-2” (b) , “3-3” (c) , “4-4” (d) , “5-5” (e) and “6-6” (f) showing self-assembled nanoparticles giving cuboids and almond shaped super-structures; insets in (c) and (d) are shown the auto organized cubic structures in case of sample “3-3” and “4-4”, respectively.

SEM images are acquired for the anhydrous NiF_2 samples and presented in Figure 10. The basic self-assemblies i.e., almond shaped big structures and the truncated bi-pyramidal sub structures observed in the SEM images of precursors (Figure 2-c, d and 3-a, b) could be clearly seen in the SEM images of their progenies (Figure 10-a – d). This is clear indication of the fact that the transformation process is secure and efficient enough to prepare NiF_2 from $NiF_2.4H_2O$ while retaining the basic shapes of the self-organized architectures. Furthermore, the SEM images support the cascade auto-organization mechanism illustrated in Figure 6. High magnification SEM images of “2-2” and “4-4” in Figure 10-b and 10-d, respectively, show the impact of dehydration process upon the surface of the self-assemblies. As could be seen in SEM images, more clearly in the case of sample “2-2”, the surfaces of self-assembled structures are marked with tiny holes. It is believed that the water molecules have escaped from the solid body through these holes. Besides the water molecules, these holes could have also been served as channels for escaping of volatile organic molecules like CF_4, C_2F_6 etc. which may be formed by the reaction of molecular F_2 with the surfactant molecules left behind after washing. The presence of limited number of surfactant molecules is evident from the FTIR spectra of samples “1” – “6” (Figure 1-b). In fact, the water and also the CF_4, C_2F_6 etc. molecules boiled off during heat treatment making small channels through the self-assembly body. This sort of porosity is also evident from the TEM images of NiF_2 samples (Figure 9), and could help in enhancing the specific surface area of the materials and be favorable for electrochemical applications (anhydrous materials will be tested as conversion based electrode material in secondary batteries).

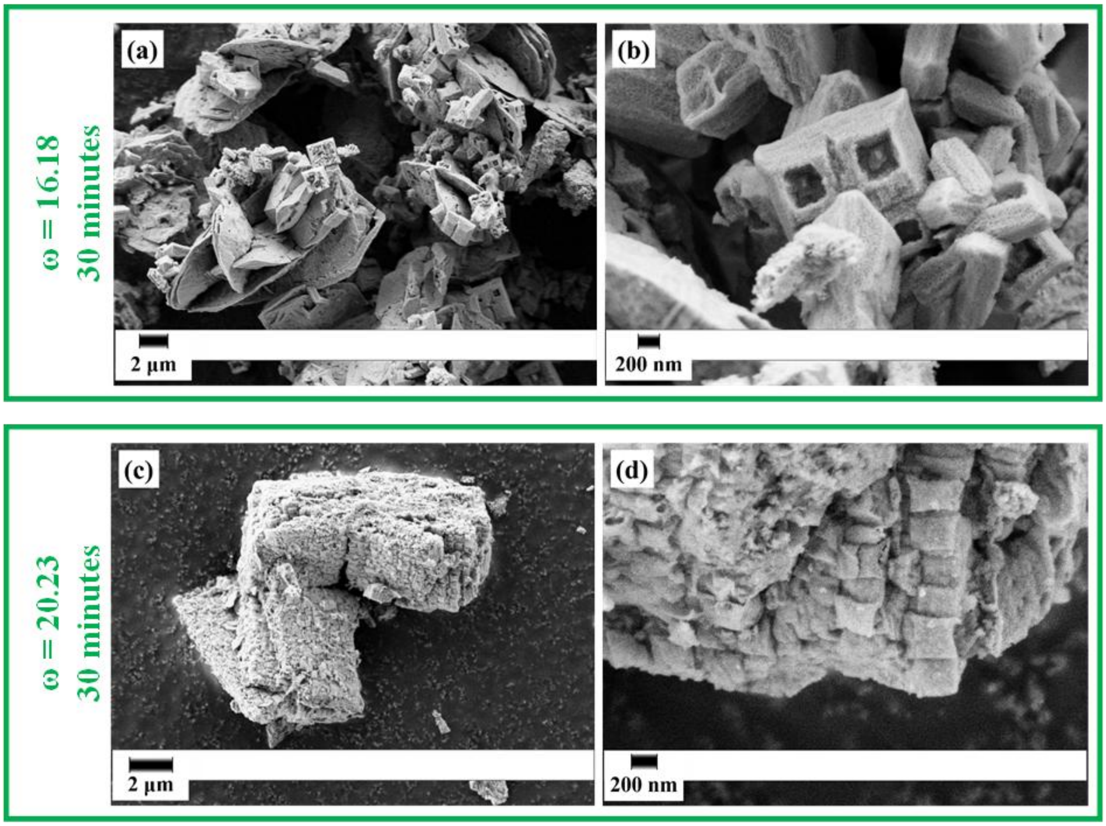

Figure 10. SEM images of dehydrated NiF_2 samples “2-2” (a, b), and “4-4” (c, d) prepared from the $NiF_2.4H_2O$ samples “2” and “4”, respectively, which were heated under vacuum at 250°C for 5 hours followed by heating under dynamic fluorine at 350°C for 5 hours.

Surface characterizations and properties:

The N_2 adsorption-desorption isotherms at 77K of the anhydrous nano-structurated NiF_2 samples (“1-1” to “6-6”) were measured employing Brunauer-Emmett-Teller (BET) method for obtaining the specific surface area and compared with bulk material (“Bulk-2”). The pertinent data are summarized in Table 3 and the N_2 sorption isotherms are presented in supplementary materials (Figure S7). The shape of adsorption-desorption isotherms for all the samples (“1-1” to “6-6”) corresponds to the type IV[71]. From the type of isotherms and the pore size distributions (insets in supplementary Figure S7), it is evident that materials of all the samples are mesoporous[71]. The developed porosity could be mainly ascribed to the interparticle spaces, and in good accordance with TEM and SEM images (Figure 9 and 10, respectively). The BET specific surface areas, and BJH (Barret-Joyner-Halenda) pore volumes and pore diameters of all the samples are comparable and are more than 60% higher than the values obtained for the bulk material. This could be attributed to the auto-organization of nanoparticles into super-structures. However, the sample “2-2” has shown maximum specific surface area and pore volumes in comparison to their analogues about 50 m²/g. This could be due to a larger number of tiny channels produced during the dehydration in case of sample “2-2” compared to their analogues and to the concomitant collapsing of the superior faces. The production of tiny holes is evident from the SEM image of sample “2-2” (Figure 10-a, b). These holes could act as diffusion channels for N_2 molecules into the body of the super-structures. The N_2 sorption isotherms profiles of the nanostructured materials also highlight the presence of mesopores with a large hysteresis between the sorption and desorption curves at high relative pressure compared to the “bulk-2” sample. That could be ascribed to the channels between the nanoparticles composing the super-structures, in good agreement with the pores volumes values obtained by the BJH method. These results show that the microemulsion synthesis allows obtaining nanomaterials with SSA about 30 m²/g (*average value*), higher more than 60% the SSA of sample obtained by a direct synthesis in aqueous HF (~18 m²/g). This value could be increased and reaches ~50 m²/g, as shown in the case of the sample “2-2”. Thanks to this synthesis method, self-assembled nano-NiF_2 samples offer an interesting surface of interaction with a surrounding medium like an electrolyte. Indeed, these interesting SSA values could be an advantage for electrochemical application, especially for the lithium diffusion.

Table 3. BET specific surfaces areas and BJH pores volumes of samples “1-1”, “2-2”, “3-3”, “4-4”, “5-5” and “6-6” prepared by the dehydration of $NiF_2.4H_2O$ nanoparticles at 250°C and 350°C under vacuum and dynamic fluorination, respectively. Comparison with NiF_2 bulk sample obtained in aqueous HF and treated in similar conditions.

Sample	**Surface Area (m^2/g) (BET)**	**Pore Vol. (cm^3/g) BJH Desorption**
“1-1”	31.7	0.079
“2-2”	51.0	0.102
“3-3”	33.2	0.076
“4-4”	24.8	0.050
“5-5”	29.1	0.076
“6-6”	15.4	0.040
“NiF_2 Bulk”	18.6	0.013

Being representative of the different samples resulting from the micro-emulsion syntheses, as well as about the organization and the morphology, than about the specific surface area, the sample “3-3” was chosen for the study of the electrochemical activity of self-assembled nano-NiF_2 materials.

The Li storage capacities and cycle performances of self-assembled nano-NiF_2 (sample “3-3”) were investigated by discharge/charge galvanostatic measurements and compared with NiF_2 bulk (bulk-2). Figures 11-a/b show the first and second discharge and charge curves of NiF_2/Li cells cycled between 1V and 4.3V at a constant current density of 10 mA/g for the chosen nanostructured material (“3-3”) compared to the bulk material ones (“Bulk 2”). The voltage profiles exhibit its electrochemical activity with a flat voltage plateau at 1.65 V for the sample “3-3” in the first discharging process (for instance the same plateau is at 1.55 V for the sample

"1-1" as seen in Figure S8. This values is higher than the value obtained for bulk material at 1.45V, meaning a lower polarization and a better lithium diffusion process in nanomaterial by comparison of bulk material. This voltage plateau, as the general voltage profile, is equivalent to the one described by Lee *et al.* for pristine and NiO-doped nickel fluoride and by Teng *et al.* for nanostructured NiF_2[46, 72]. The first discharge capacity of nano-NiF_2 is about 650 mAh/g and is higher than the theoretical value of 554 mAh/g. This is explained by a concomitant redox mechanism of NiF_2 and the formation of a Solid Electrolyte Interface (SEI)[46]. The irreversible capacity leading to SEI is directly proportional to the SSA. As the nanostructured materials "1-1" and "3-3" have about the same SSA, their SEI are attempted to be the same leading to the same discharge capacity (see Figure S8 for sample "1-1"). In parallel, since the SSA of bulk NiF_2 is lower than the one of the nanostructured compounds, only a fewer irreversible capacity can contribute to the first reduction capacity. Moreover, the first reduction capacity of the bulk material is lower than the theoretical value, so lithium diffusion process may be limited the access to the overall active material. A better diffusion of the lithium ions in the more opened structures of the self-organized NiF_2 nanoparticles compared with the bulk compound (see Figure 11-b) can explain the higher value of the second reduction capacity for "3-3" sample than NiF_2 bulk.

In the literature, two different mechanisms have been proposed concerning the electrochemical activity of NiF_2. In their studies, Dae Hoe Lee *et al.* have described a conversion mechanism supported by XAS and XRD measurements[46, 73]. According the authors, the first cycle profile appears as different as the second one because of a conversion mechanism of NiF_2 into Ni during which the NiF_2 particles are electrochemically ground and reduced into little particles of nickel. Then the following oxidation gives heterogeneous NiF_2 particles with different electrochemical potentials. So no flatter plateau of NiF_2 can be obtained during the second reduction process. In another side, a study of Zhang et al. [7] made on NiF_2 nanoparticles about of 20-30 nm in size deposited by pulse laser deposition shows good electrochemical performances for NiF_2 used as cathode in lithium batteries (more than 40 cycles and a delivered capacity higher than 400 mAh/g between 3.5V and 0V), because of the stabilization of Li_2NiF_4 as an intermediate during the reversible electrochemical reaction of NiF_2 with Li. The galvanostatic curves of our samples (nanostructured and bulk) are very similar with those presented in the studies of Lee et *al.*, and are dissimilar to those reported by Zhang et al. This is the case on the plateau values during the first discharge or on next cycles. To confirm the electrochemical mechanism of our NiF_2 samples (bulk and nanostructured “3-3” sample), the changes of the oxidation state of nickel have been followed by XAS thanks several galvanostatic measurements with various cutoff voltage at 1.5 and 1.0V in reduction and 1.5, 3.2, 4.0 and 4.3V over the first and second cycles (Figure 11-c/d). In the case of the bulk material, the Ni K-edge energy varies between 8344 and 8339.6 eV during the reduction, whereas in the case of sample “3-3” a minimum of 8338 eV for the same edge is obtained. This last minimum is narrower to the attempted value of metallic nickel at 8333 eV[73]. It demonstrates that more metallic nickel amount is obtained for nanomaterial than for bulk sample. This result shows that the electrochemical mechanisms of our bulk and nanostructured NiF_2 are quite the same, that is to say a conversion process to metallic nickel and that demonstrating a better efficiency of formation of metallic nickel for the nanostructured material than the bulk one[73]. Moreover, it demonstrates also that no reaction between Ni and LiF occurred to stabilize nickel into Li_2NiF_4 as at the end of oxidation[74], the recovering of starting spectra is obtained in both cases. Indeed, the XANES region is mostly determined by valence, the symmetry of the local environment, and the nearest neighbor bond length. As Li_2NiF_4 structure is

Fd3m and the one of NiF_2 is $P4_2/mnm$, one can conclude that the formation of Li_2NiF_4 is avoided. So, our synthesized (nano)-particles do not favor the formation of the Li_2NiF_4 phase and exhibit an electrochemical behavior very similar with the conversion mechanism proposed by Lee et al. with a rapid decrease of the capacity after only two cycles due to the SEI formation during the first cycle. Nevertheless, the values of capacities reached by nanostructured NiF_2 are higher than those relatives to the bulk compound. These results give evidences that NiF_2 organization into self-assembled nanostructures appears to be more favorable than dense and bulk structures for its electrochemical activity.

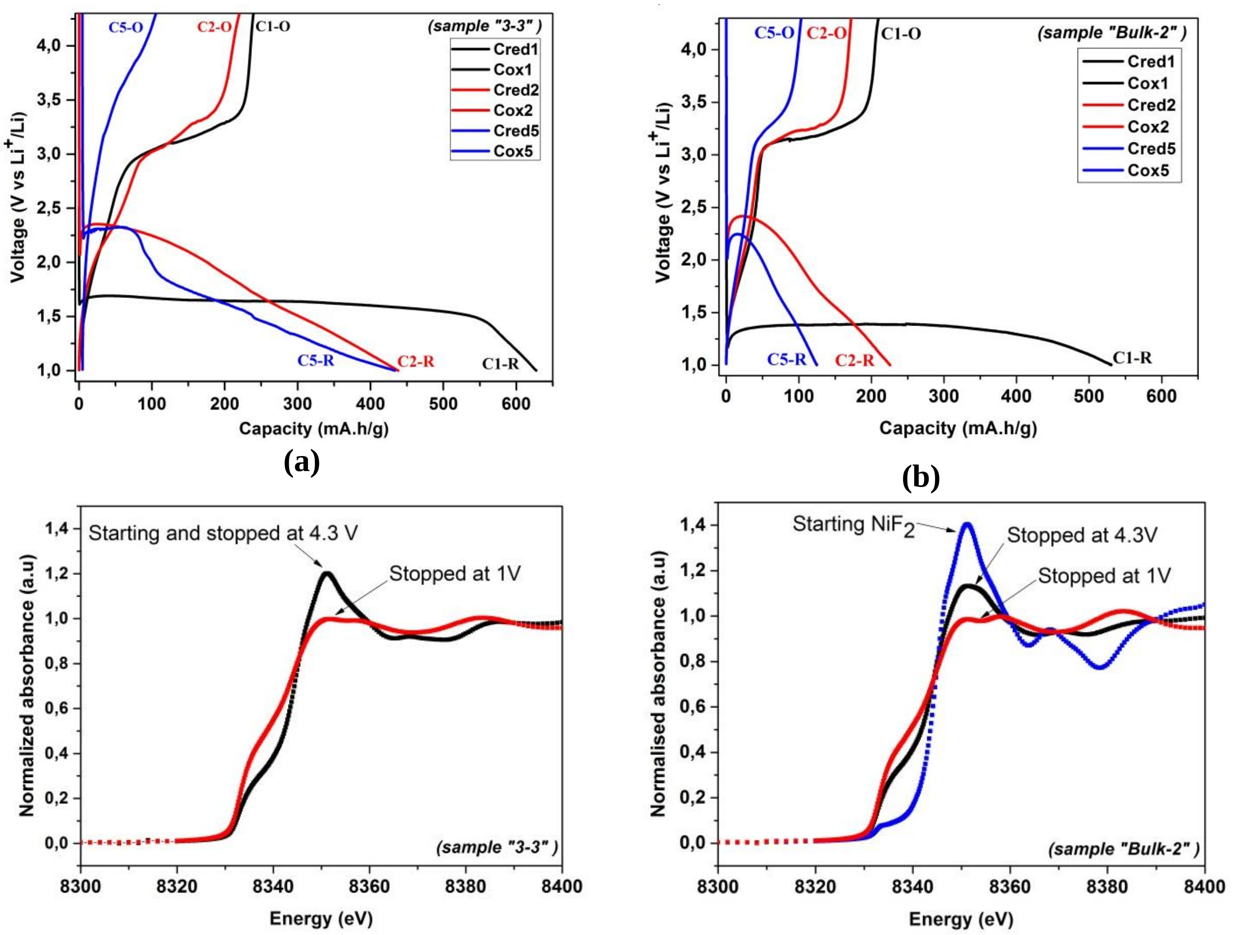

Figure 11. First, second and fifth galvanostatic cycles of half-cells using as cathode material sample “3-3” (a) compared to those of bulk material (*sample “bulk-2”*) (b). Oxidation and reduction process are labeled “Cox” and “Cred” respectively. XANES spectra of the nanostructured “3-3” (c) and bulk (*sample “bulk-2”*) (d) NiF_2 electrode materials before electrochemical measurements or after 1 full cycle and 1 reduction, stopped at 4.3 V or 1V.

Magnetic characterizations:

The magnetic properties of the samples “bulk-1” and “bulk-2”, and of nanoparticles samples “1”, “6”, “1-1” and “6-6” were investigated under a 5000 Oe dc magnetic field in zero-field-cooled (ZFC) mode in the temperature range 1.8 – 300 K. The molar magnetic susceptibilities curves as a function of temperature for samples “bulk-1”, “1” and “6” are given in Figure 12-a, and for samples “bulk-2”, “1-1” and “6-6” in Figure 12-b. The inverse of the susceptibility curves can be fitted by the Curie-Weiss law in the high temperature region (above 150 K) (shown in Fig S9 (a-f)), which provides Curie constants around 1.36 $emu\cdot K\cdot mol^{-1}$ for the hydrated compounds (“bulk-1”, sample “1” and sample “6”) and slightly larger, around 1.41 $emu\cdot K\cdot mol^{-1}$, for the dehydrated compounds (“bulk-2”, sample “1-1” and sample “6-6”). These values of the Curie constant are well consistent with the expected value for the Ni (II) ion (~ 1.3 $emu.K\cdot mol^{-1}$) in octahedral geometry and the value about 1.36 $emu.K\cdot mol^{-1}$ found for NiF_2 by Cooke et al.[75]. The Weiss temperatures are negative (around -8.7 K for the hydrated samples, and around -130 K for the dehydrated samples), which indicates the occurrence of dominant antiferromagnetic interactions, much larger in the case of the dehydrated samples. The ZFC curves for samples “bulk-1”, “1” and “6” show a single and relatively sharp peak around 3.8 K which indicates the occurrence of antiferromagnetic ordering. It is worth noticing that to the best of our knowledge, it is the first time the magnetic behavior of $NiF_2.4H_2O$ is reported. No influence of the size reduction and self-assembly can be noticed.

The ZCF curves of anhydrous NiF_2 ("bulk-2", sample "1-1" and sample "2-2") show two peaks at ~4 K and ~74 K. The peak at 74 K corresponds to the already reported Néel temperature of NiF_2[75-76]. There again, no change of the magnetic properties of NiF_2 nanoparticles compared to their bulk counterpart can be noticed, most probably because the size of the obtained nanoparticles is still too large to detect any significant size reduction effect. Indeed, the modeling work of Lang et al.[77] shows that in the case of NiF_2, the effects of reducing the Néel temperature with the particle size become significant only for nanoparticle sizes smaller than 10 nm. In our case, the smallest NiF_2 particles have sizes of the order of 24 nm and monocrystalline domains of 13 nm. Again, no noticeable influence of self-assembly is observed. The emergence of a second peak around 4 K is rather surprising and likely corresponds to the presence of a small quantity of $NiF_2.4H_2O$ that could be probably due to a slight hydration of the compounds before measurement

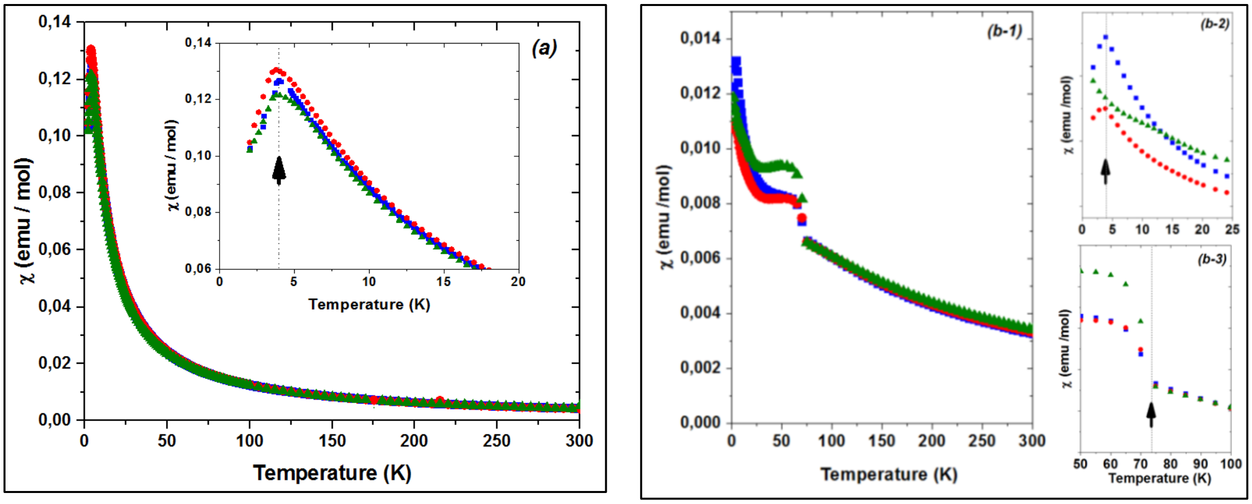

Figure 12. (a) χ = f(T) curves for “bulk-1” (blue), sample “1” (red) and sample “6” (green), and (b) “bulk-2” (blue), sample “1-1” (red) and sample “6-6” (green) under a 5000 Oe dc magnetic field (zfc mode). Insert in figure (a) is a zoom around 4K for hydrated compounds, while figures (b-2) and (b-3) are zooms around 4K and 74K respectively for anhydrous compounds.

CONCLUSION

Obtaining self-assembled nanoparticles of anhydrous metal fluoride is a real challenge. Indeed, most of fluorides of transition metal present hydrated forms, but in the same time nanostructuration with self-assembly is generally obtained in aqueous media. In this paper, microemulsion method has been used for the first time to make self-assembled nanoparticles of $NiF_2.4H_2O$ and the obtained compounds have been successfully converted into anhydrous NiF_2 while preserving self-assemblies thanks to controlled gas/solid fluorination.

The influence of the synthesis parameters of the water-in-oil microemulsion method, such as time or water/2-octanol ratio has been studied. The control of these parameters does not change strongly the size and the shape of the individual nanoparticles, even a small increase as a result of increasing the reaction time and the water to octanol ratio of the microemulsions. The morphological studies revealed an assembly mechanism made by a cascade of auto-organization process from the primary auto-organization of the individual nanoparticles into layers which packed together to give tiny cubes to their self-assembly giving truncated bipyramids. The preferential plane growth mechanism for the successive assemblies leads the formation of large almond-like super-structures. Unlike the formation of the individual nanoparticles, the synthesis parameters have a significant influence on their self-assembly. The water/2-octanol ratio (α) drives the primary auto-organization of the individual nanoparticles while the super-structures size depends on the reaction time. The controlled post-treatment of fluorination under molecular fluorine allows transforming hydrated nickel fluoride nanoparticles into anhydrous particles without destruction of the self-assembled structures. The self-assembled structure and the water released by fluorination lead to noticeable surface areas which promote better Li^+ diffusion during charge/discharge of the LIBs compared with bulk NiF_2. The electrochemical activity of the self-assembled materials has been investigated and compared with bulk sample, it clearly shows the importance of the nano-structuration on the SEI formation along the redox process of NiF_2. The electrochemical conversion mechanism is confirmed XAS measurements and the discharges capacities are in good agreement with values presented in the literature. Finally, the magnetic characterizations of nanostructured hydrated (for the first time) and anhydrous NiF_2 show the same behaviors than the bulk materials, without any noticeable size-reduction and self-assembly effect.

This paper shows that our combined synthesis method (microemulsion + fluorination) has high potential for making self-assembled nanosized anhydrous nickel fluoride. It appears to be very promising for the controlled synthesis of anhydrous functional fluorides with the mutual benefits of nanostructuration, self-assembly and water-free compounds. This study opens way for future works concentrated upon the electrochemical studies of the self-assembled materials and the optimization the charge/discharge process.

SUPPORTING INFORMATION

Synthesis of $NiF_2.4H_2O$ at low water to oil ratio (α~0.7). Synthesis of $NiF_2.4H_2O$ AND NiF_2 (Synthesis parameters, TGA, fluorination and TEM pictures). Isotherms and the pore size distributions of NiF_2 samples. First Galvanostatic cycle of half cell using as cathode material sample “1-1”. Magnetic characterizations and properties of samples “1”, “6”, “1-1” “6-6”AND “bulk-1” and “bulk-2”.

ACKNOWLEDGEMENTS

We sincerely acknowledge Higher Education Commission (HEC) of Pakistan, Campus France and Embassy of France in Pakistan for granting post-doctoral fellowship to one of the authors (Dr. Hameed Ullah) under the program “2014 HEC and French Embassy Split PhD and Post-Doc Scholarship Programme”. We thank Mr. Fabien Veillon and Dr. Alain Pautrat (CRISMAT, Caen), for their help with some magnetic measurements. The authors thank the platform Centre Imagerie Cellulaire Sante (Clermont Auvergne University), most notably Christelle Blavignac, for her technical assistance in TEM analysis. We thank all people of ICCF who help on this study: Mr. Joel Cellier (ICCF) and Rodolphe Thirouard (ICCF) for XRD and TGA/DSC analysis, respectively; Dr. Lea Doubtsof (ICCF) and Yin Zhang are thanked for electrochemical tests; Pr. Mohammad Sarakha (ICCF) for his help in DRS measurements and to Dr. Diane Delbegue (ICCF), Dr. Fabrice Leroux (ICCF) and Dr. Stephanie Belin (Synchrotron SOLEIL - Rock Line) for helping us on XAS measurements and analyses. Our sincere thanks go to Synchrotron SOLEIL for the beam time allowed on the Rock line.

REFERENCES

1. Goldberger, J.; He, R.; Zhang, Y.; Lee, S.; Yan, H.; Choi, H.-J.; Yang, P., Single-crystal gallium nitride nanotubes. *Nature* **2003,** *422* (6932), 599.

2. Perepichka, D. F.; Rosei, F., Metal nanoparticles: From “artificial atoms” to “artificial molecules”. *Angew. Chem., Int. Ed.* **2007,** *46* (32), 6006-6008.

3. Liu, J.; Xue, D., Hollow nanostructured anode materials for Li-ion batteries. *Nanoscale. Res. Lett.* **2010,** *5* (10), 1525.

4. Liu, J.; Xia, H.; Xue, D.; Lu, L., Double-shelled nanocapsules of V_2O_5-based composites as high-performance anode and cathode materials for Li ion batteries. *J. Am. Chem. Soc.* **2009,** *131* (34), 12086-12087.

5. Liu, J.; Liu, F.; Gao, K.; Wu, J.; Xue, D., Recent developments in the chemical synthesis of inorganic porous capsules. *J. Mater. Chem.* **2009,** *19* (34), 6073-6084.

6. Ullah, H.; Khatoon, A.; Akhtar, Z., Synthesis and photocatalytic study of SnO_2/Zn_2SnO_4 nanocomposite prepared by sol–gel method using single source molecular precursor. *Mater. Res. Express* **2014,** *1* (4), 045001.

7. Zhang, H.; Zhou, Y.-N.; Sun, Q.; Fu, Z.-W., Nanostructured nickel fluoride thin film as a new Li storage material. *Solid. State Sci.* **2008,** *10* (9), 1166-1172.

8. Fedorov, P. P.; Luginina, A. A.; Kuznetsov, S. V.; Osiko, V. V., Nanofluorides. *J. Fluorine Chem.* **2011,** *132* (12), 1012-1039.

9. Tarascon, J.-M.; Armand, M., Issues and challenges facing rechargeable lithium batteries. In *Materials for Sustainable Energy: A Collection of Peer-Reviewed Research and Review Articles from Nature Publishing Group*, World Scientific: 2011; pp 171-179.

10. Bruce, P. G.; Scrosati, B.; Tarascon, J. M., Nanomaterials for rechargeable lithium batteries. *Angew. Chem., Int. Ed.* **2008,** *47* (16), 2930-2946.

11. Armand, M.; Tarascon, J.-M., Building better batteries. *Nature* **2008,** *451* (7179), 652.

12. Kuzyk, A.; Schreiber, R.; Fan, Z.; Pardatscher, G.; Roller, E.-M.; Högele, A.; Simmel, F. C.; Govorov, A. O.; Liedl, T., DNA-based self-assembly of chiral plasmonic nanostructures with tailored optical response. *Nature* **2012,** *483* (7389), 311.

13. Henry, E.; Dif, A.; Schmutz, M.; Legoff, L.; Amblard, F.; Marchi-Artzner, V.; Artzner, F., Crystallization of fluorescent quantum dots within a three-dimensional bio-organic template of actin filaments and lipid membranes. *Nano Lett.* **2011,** *11* (12), 5443-5448.

14. Zhang, Y.; Lu, F.; Yager, K. G.; Van Der Lelie, D.; Gang, O., A general strategy for the DNA-mediated self-assembly of functional nanoparticles into heterogeneous systems. *Nat. Nanotechnol.* **2013,** *8* (11), 865.

15. Hoffelner, D.; Kundt, M.; Schmidt, A. M.; Kentzinger, E.; Bender, P.; Disch, S., Directing the orientational alignment of anisotropic magnetic nanoparticles using dynamic magnetic fields. *Faraday Discuss.* **2015,** *181*, 449-461.

16. Alivisatos, A. P., Semiconductor clusters, nanocrystals, and quantum dots. *Science* **1996,** *271* (5251), 933-937.

17. Yin, J.; Wang, Z., In situ structural evolution of self-assembled oxide nanocrystals. *J. Phys. Chem. B* **1997,** *101* (44), 8979-8983.

18. Barringer, E. A.; Bowen, H. K., Formation, packing, and sintering of monodisperse TiO_2 powders. *J. Am. Ceram. Soc.* **1982,** *65* (12), C199-C201.

19. Kitching, H.; Shiers, M. J.; Kenyon, A. J.; Parkin, I. P., Self-assembly of metallic nanoparticles into one dimensional arrays. *J. Mater. Chem. A* **2013,** *1* (24), 6985-6999.

20. Mohl, M.; Dombovari, A.; Vajtai, R.; Ajayan, P. M.; Kordas, K., Self-assembled large scale metal alloy grid patterns as flexible transparent conductive layers. *Sci. Rep.* **2015,** *5*, 13710.

21. Siffalovic, P.; Majkova, E.; Chitu, L.; Jergel, M.; Luby, S.; Satka, A.; Roth, S., Self-assembly of iron oxide nanoparticles studied by time-resolved grazing-incidence small-angle x-ray scattering. *Phys. Rev. B* **2007,** *76* (19), 195432.

22. Tsuruoka, T.; Kawasaki, H.; Nawafune, H.; Akamatsu, K., Controlled self-assembly of metal–organic frameworks on metal nanoparticles for efficient synthesis of hybrid nanostructures. *ACS Appl. Mater. Inter.* **2011,** *3* (10), 3788-3791.

23. Peng, X.; Manna, L.; Yang, W.; Wickham, J.; Scher, E.; Kadavanich, A.; Alivisatos, A. P., Shape control of CdSe nanocrystals. *Nature* **2000,** *404* (6773), 59.

24. Whitesides, G. M.; Grzybowski, B., Self-assembly at all scales. *Science* **2002,** *295* (5564), 2418-2421.

25. Rycenga, M.; McLellan, J. M.; Xia, Y., Controlling the assembly of silver nanocubes through selective functionalization of their faces. *Adv. Mater.* **2008,** *20* (12), 2416-2420.

26. Lu, F.; Yager, K. G.; Zhang, Y.; Xin, H.; Gang, O., Superlattices assembled through shape-induced directional binding. *Nat. Commun.* **2015,** *6*, 6912.

27. Talapin, D. V.; Shevchenko, E. V.; Murray, C. B.; Titov, A. V.; Kral, P., Dipole− dipole interactions in nanoparticle superlattices. *Nano Lett.* **2007,** *7* (5), 1213-1219.

28. Burnside, S. D.; Shklover, V.; Barbé, C.; Comte, P.; Arendse, F.; Brooks, K.; Grätzel, M., Self-organization of TiO_2 nanoparticles in thin films. *Chem. Mater.* **1998,** *10* (9), 2419-2425.

29. Li, M.; Schnablegger, H.; Mann, S., Coupled synthesis and self-assembly of nanoparticles to give structures with controlled organization. *Nature* **1999,** *402* (6760), 393.

30. Kipouros, G.; Flengas, S., Electrorefining of zirconium metal in alkali chloride and alkali fluoride fused electrolytes. *J. Electrochem. Soc.* **1985,** *132* (5), 1087-1098.

31. Herbst, R.; McCandless, F., Improved donors for the separation of the boron isotopes by gas-liquid exchange reactions. *Sep. Sci. Technol.* **1994,** *29* (10), 1293-1310.

32. Ohishi, Y.; Mitachi, S.; Kanamori, T.; Manabe, T., Optical absorption of 3d transition metal and rare earth elements in zirconium fluoride glasses. *Phys. Chem. Glasses.* **1983,** *24* (5), 135-140.

33. Fergus, J. W., The application of solid fluoride electrolytes in chemical sensors. *Sensor Actuat. B-Chem.* **1997,** *42* (2), 119-130.

34. Delcet, J.; Heus, R.; Egan, J., Electronic conductivity in solid CaF_2 at high temperature. *J. Electrochem. Soc.* **1978,** *125* (5), 755-758.

35. Zhang, Z.; Yu, L.; Liu, W.; Xue, Q., The effect of LaF_3 nanocluster modified with succinimide on the lubricating performance of liquid paraffin for steel-on-steel system. *Tribol. Int.* **2001,** *34* (2), 83-88.

36. Jost, H. P., Tribology: The First 25 Years and Beyond-Achievements, Shortcomings and Future Tasks [tribology, as a word and concept, was first enunciated in a British Government Report, published on 9 March 1966(Jost Report)]. *Ind. Lubr. Tribol.* **1992,** *44* (2), 6.

37. Qiu, S.; Dong, J.; Chen, G., Synthesis of CeF_3 nanoparticles from water-in-oil microemulsions. *Powder. Technol.* **2000,** *113* (1-2), 9-13.

38. Hua, R.; Zang, C.; Shao, C.; Xie, D.; Shi, C., Synthesis of barium fluoride nanoparticles from microemulsion. *Nanotechnology* **2003,** *14* (6), 588.

39. Ganguli, A. K.; Ganguly, A.; Vaidya, S., Microemulsion-based synthesis of nanocrystalline materials. *Chem. Soc. Rev.* **2010,** *39* (2), 474-485.

40. Kitchens, C. L.; McLeod, M. C.; Roberts, C. B., Chloride ion effects on synthesis and directed assembly of copper nanoparticles in liquid and compressed alkane microemulsions. *Langmuir* **2005,** *21* (11), 5166-5173.

41. Shi, H.; Qi, L.; Ma, J.; Cheng, H., Polymer-directed synthesis of penniform $BaWO_4$ nanostructures in reverse micelles. *J. Am. Chem. Soc.* **2003,** *125* (12), 3450-3451.

42. Vaucher, S.; Li, M.; Mann, S., Synthesis of Prussian blue nanoparticles and nanocrystal superlattices in reverse microemulsions. *Angew. Chem., Int. Ed.* **2000,** *39* (10), 1793-1796.

43. Lemyre, J.-L.; Ritcey, A. M., Synthesis of lanthanide fluoride nanoparticles of varying shape and size. *Chem. Mater.* **2005,** *17* (11), 3040-3043.

44. Zhang, N.; Xiao, X.; Pang, H., Transition metal (Fe, Co, Ni) fluoride-based materials for electrochemical energy storage. *Nanoscale Horiz.* **2019,** *4* (1), 99-116.

45. Amatucci, G. G.; Pereira, N., Fluoride based electrode materials for advanced energy storage devices. *J. Fluorine Chem.* **2007,** *128* (4), 243-262.

46. Lee, D. H.; Carroll, K. J.; Calvin, S.; Jin, S.; Meng, Y. S., Conversion mechanism of nickel fluoride and NiO-doped nickel fluoride in Li ion batteries. *Electrochim. Acta.* **2012,** *59*, 213-221.

47. Su, D.; Xie, X.; Dou, S.; Wang, G., CuO single crystal with exposed {001} facets-A highly efficient material for gas sensing and Li-ion battery applications. *Sci. Rep.* **2014,** *4*, 5753.

48. Billas, I. M.; Becker, J.; Châtelain, A.; de Heer, W. A., Magnetic moments of iron clusters with 25 to 700 atoms and their dependence on temperature. *Phys. Rev. Lett.* **1993,** *71* (24), 4067.

49. Berdonosov, S. S.; Lebedev, V. Y.; Berdonosova, D. G.; Prokofiev, M. A.; Znamenskaya, I. V.; Melikhov, I. V.; Kharisov, B. I.; Méndez, U. O.; Kharissova, O. V., Influence of Microwave Treatment on the Dehydration of Crystallohydrates of Iron, Cobalt and Nickel Flourides. *J. Microwave. Power. EE.* **2007,** *42* (2), 15-20.

50. Boutonnet, M.; Kizling, J.; Stenius, P.; Maire, G., The preparation of monodisperse colloidal metal particles from microemulsions. *Colloid. Surface.* **1982,** *5* (3), 209-225.

51. Moulik, S. P.; Paul, B. K., Structure, dynamics and transport properties of microemulsions. *Adv. Colloid Interface Sci.* **1998,** *78* (2), 99-195.

52. Rossman, G. R.; Shannon, R. D.; Waring, R. K., Origin of the yellow color of complex nickel oxides. *J. Solid State Chem.* **1981,** *39* (3), 277-287.

53. Roth, M.; Hempelmann, R.; Borgmeier, O.; Eifert, T.; Lueken, H., Nanocrystalline NH_4MnF_3 with controlled grain size: Synthesis and antiferromagnetism. *Nanostruct. Mater.* **1999,** *12* (5-8), 855-858.

54. Qi, L., Synthesis of inorganic nanostructures in reverse micelles. *Encyclopedia of Surface and Colloid Science* **2006,** *2*, 6183-6207.

55. Eastoe, J.; Hollamby, M. J.; Hudson, L., Recent advances in nanoparticle synthesis with reversed micelles. *Adv. Colloid Interfac. Sci.* **2006,** *128,* 5-15.

56. Chandradass, J.; Balasubramanian, M.; Bae, D. S.; Kim, J.; Kim, K. H., Effect of water to surfactant ratio (R) on the particle size of $MgAl_2O_4$ nanoparticle prepared via reverse micelle process. *J. Alloy. Compd.* **2010,** *491* (1-2), L25-L28.

57. Petit, C.; Lixon, P.; Pileni, M. P., In situ synthesis of silver nanocluster in AOT reverse micelles. *J. Phys. Chem.* **1993,** *97* (49), 12974-12983.

58. Patil, K.; Secco, E., Metal halide ammines. II. Thermal analyses, calorimetry and infrared spectra of fluoride ammines and hydrates of bivalent metals. *Can. J. Chem.* **1972,** *50* (4), 567-573.

59. Taibi, M.; Ammar, S.; Jouini, N.; Fiévet, F.; Molinié, P.; Drillon, M., Layered nickel hydroxide salts: synthesis, characterization and magnetic behaviour in relation to the basal spacing. *J. Mater. Chem.* **2002,** *12* (11), 3238-3244.

60. Poul, L.; Jouini, N.; Fiévet, F., Layered hydroxide metal acetates (metal= zinc, cobalt, and nickel): elaboration via hydrolysis in polyol medium and comparative study. *Chem. Mater.* **2000,** *12* (10), 3123-3132.

61. Mayo, D. W.; Miller, F. A.; Hannah, R. W., *Course notes on the interpretation of infrared and Raman spectra*. John Wiley & Sons: 2004.

62. Jiang, Z.; Xie, J.; Jiang, D.; Wei, X.; Chen, M., Modifiers-assisted formation of nickel nanoparticles and their catalytic application to p-nitrophenol reduction. *CrystEngComm* **2013,** *15* (3), 560-569.

63. Hutchings, M.; Thorpe, M.; Birgeneau, R.; Fleury, P.; Guggenheim, H., Neutron and Optical Investigation of Magnons and Magnon-Magnon Interaction Effects in NiF_2. *Phys. Rev. B* **1970,** *2* (5), 1362.

64. Agulló Rueda, F.; Calleja, J.; Martini, M.; Spinolo, G.; Cariati, F., Raman and infrared spectra of transition metal halide hexahydrates. *J. Raman. Spectrosc.* **1987,** *18* (7), 485-491.

65. Scherer, J. R.; Go, M. K.; Kint, S., Raman spectra and structure of water from-10 to 90. deg. *J. Phys. Chem.* **1974,** *78* (13), 1304-1313.

66. Stout, J.; Reed, S. A., The crystal structure of MnF_2, FeF_2, CoF_2, NiF_2 and ZnF_2. *J. Am. Chem. Soc.* **1954,** *76* (21), 5279-5281.

67. Klug, H. P.; Alexander, L. E., X-ray diffraction procedures: for polycrystalline and amorphous materials. *X-Ray Diffraction Procedures: For Polycrystalline and Amorphous Materials, 2nd Edition, by Harold P. Klug, Leroy E. Alexander, pp. 992. ISBN 0-471-49369-4. Wiley-VCH, May 1974.* **1974**, 992.

68. Tramšek, M.; Žemva, B., Higher fluorides of nickel: Syntheses and some properties of Ni_2F_5. *Acta. Chim. Slov.* **2002,** *49*, 209-220.

69. da Silva Jr, E.; Machado, F.; Rezende, S., High resolution Raman scattering by phonons in FeF_2 and NiF_2. *Solid State Commun.* **1983,** *48* (12), 1077-1079.

70. Dieguez, A.; Romano-Rodrıguez, A.; Vila, A.; Morante, J., The complete Raman spectrum of nanometric SnO_2 particles. *J. Appl. Phys.* **2001,** *90* (3), 1550-1557.

71. Vinayan, B.; Sethupathi, K.; Ramaprabhu, S., Facile synthesis of triangular shaped palladium nanoparticles decorated nitrogen doped graphene and their catalytic study for renewable energy applications. *Int. J. Hydrogen. Energ.* **2013,** *38* (5), 2240-2250.

72. Teng, Y. T.; Wei, F.; Yazami, R., Synthesis of $Ni_xCo_{(1-x)}F_2$ (x= 0, 0.25, 0.50, 0.75, 1.0) and application in lithium ion batteries. *J. Alloy. Compd.* **2015,** *653*, 434-443.

73. Lee, D. H.; Carroll, K. J.; Chapman, K. W.; Borkiewicz, O. J.; Calvin, S.; Fullerton, E. E.; Meng, Y. S., Understanding improved electrochemical properties of NiO-doped NiF_2–C

composite conversion materials by X-ray absorption spectroscopy and pair distribution function analysis. *Phys. Chem. Chem. Phys.* **2014,** *16* (7), 3095-3102.

74. Lieser, G.; de Biasi, L.; Scheuermann, M.; Winkler, V.; Eisenhardt, S.; Glatthaar, S.; Indris, S.; Geßwein, H.; Hoffmann, M. J.; Ehrenberg, H., Sol-Gel Processing and Electrochemical Conversion of Inverse Spinel-Type Li_2NiF_4. *J. Electrochem. Soc.* **2015,** *162* (4), A679-A686.

75. Cooke, A.; Gehring, K.; Lazenby, R., The magnetic properties of NiF_2. *P. Phys. Soc.* **1965,** *85* (5), 967.

76. Brown, P.; Forsyth, J., A neutron diffraction study of weak ferromagnetism in nickel fluoride. *J. Phys. C Solid State* **1981,** *14* (33), 5171.

77. Lang, X.; Wen, Z.; Jiang, Q., Dependence of Thermal Stability of Antiferromagnetic Nanocrystals on Size and Magnetic Proximity Effect. *J. Phys. Chem. C* **2008,** *112* (11), 4055-4060.

Table of Contents (TOC)/Abstract Graphic